ABSTRACT

Title of thesis: ANALYSIS OF FACTORS AFFECTING THE AERODYNAMICS OF LOW REYNOLDS NUMBER ROTATING WINGS

Kristy Schlueter, Master of Science, 2013

Thesis directed by: Professor Anya Jones
Department of Aerospace Engineering

A computational analysis was performed to address the effects of walls on wings rotating at a Reynolds number of 120. For rotation angles less than one revolution, a tip clearance of 0.5 chord-lengths is sufficient to approximate a wing rotating in an infinitely large volume of fluid. However, for a maximum rotation of two revolutions, a tip clearance of 5.0 chords is necessary. At the start of the second revolution, the wing encounters its wake, and the wake structure is significantly affected by low tip clearances.

Lift and drag forces were measured experimentally for wings rotating at a Reynolds number of 10,000 while parameters including root cutout were varied. Root cutout significantly alters the lift and drag coefficients, including the location of a second local maximum in both lift and drag. The root-relative method of force non-dimensionalization provided the best comparison of force coefficients between cases with different root cutouts.

ANALYSIS OF FACTORS AFFECTING THE AERODYNAMICS OF LOW REYNOLDS NUMBER ROTATING WINGS

by

Kristy Lynn Schlueter

Thesis submitted to the Faculty of the Graduate School of the
University of Maryland, College Park in partial fulfillment
of the requirements for the degree of
Master of Science
2013

Advisory Committee:
Professor Anya Jones, Chair/Advisor
Professor James Baeder
Professor Sean Humbert

Acknowledgments

I would like to express my sincere appreciation to my advisor, Dr Anya Jones for her guidance and support throughout my degree program. I have greatly enjoyed working in her lab, and have learned and grown immensely under her leadership since the start of my program. I would also like to acknowledge Mac MacFarlane for his assistance with the computational side of this research, as well as the past and present graduate students in the Jones Aerodynamics Lab for their help with various aspects of this project. Lastly, I would like to thank my friends and family for their continued love and support, their willingness to listen to me talk about my research, and their encouragement over the last several years.

Table of Contents

List of Tables

List of Figures

Nomenclature

α	Angle of attack, deg
Γ	Circulation of a vortex
γ	Vortex detection parameter, see Eqn. 3.2
μ	Dynamic viscosity, kg/(m·s)
ν	Kinematic viscosity, m^2/s
θ	Rotation angle, deg
Ω	Angular velocity, rad/s
ω	vorticity, s^{-1}
b	Span, m
c	Wing chord, m
C_F	Total force coefficient
C_L	Lift coefficient
C_D	Drag coefficient
d_b	Tip clearance, m
D	Drag, N
L	Lift, N
Q	Vortex detection parameter, see Eqn 3.1
Re	Reynolds number, $U_{ref}c/\nu$
r_r	Root radius, distance from axis of rotation to wing root, m
r_t	Tip radius, distance from axis of rotation to wing tip, m
s	Distance traveled at reference plane, m
t	Time, s
U_{ref}	Reference velocity, m/s
AFRL	Air Force Research Lab
AR	Aspect Ratio, b/c
CFD	Computational Fluid Dynamics
IBINS	Immersed Boundary Implicit Navier-Stokes Solver
LE	Leading Edge
LEV	Leading Edge Vortex
MAV	Micro Air Vehicle
PIV	Particle Image Velocimetry
TE	Trailing Edge
TEV	Trailing Edge Vortex
UMD	University of Maryland, College Park

Chapter 1

Introduction

1.1 Overview

Recent advancements in small scale surveillance equipment, including miniaturized cameras, has prompted interest in the development of stable, maneuverable micro air vehicles (MAVs) on which to put them. One MAV model mimics the flapping kinematics of insects and small birds capable of hovering. Although these animals are capable of sustained hovering, recover quickly from large gust loads, and are extremely maneuverable, the underlying aerodynamics of these motions are poorly understood.

1.2 MAV Concepts

Other MAV concepts have included fixed wing aircraft and rotorcraft designs, as shown in Figure 1.1. The left image (a) shows the Aerovironment fixed wing Black Widow [1], measuring 6 in across, while the right image (b) shows a shrouded rotor concept known as TiShrov-2 developed at the University of Maryland [2]. However, both of these concepts have significant disadvantages. While fixed wing aircraft have high endurance and efficiency, they are not capable of hovering. Rotorcraft-based MAVs, however and are relatively efficient when compared to insect wing flapping,

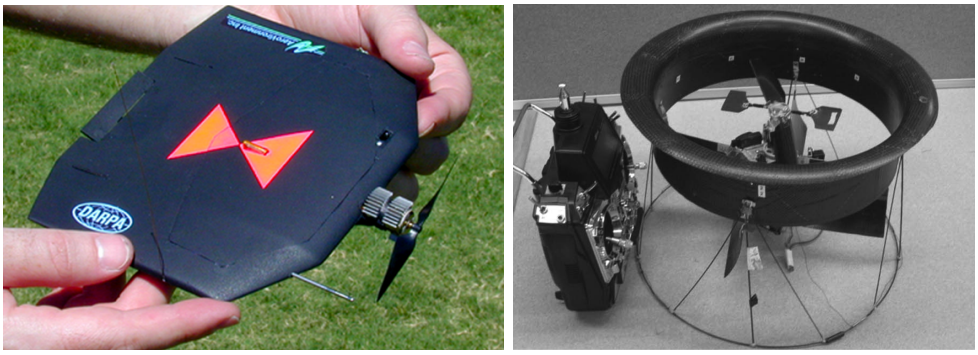

(a) Black widow [2] (b) TiShrov-2 shrouded rotor [1]

Figure 1.1: MAV concepts.

but are not capable of quick and stable recovery from gust loading. Insects are both capable of hovering and able to recover from very high gust loads in just a few wingbeats. Ideally, MAV models based on insect flapping would have these same characteristics.

1.3 Flapping Kinematics

The basic kinematics of insect wing flapping can be broken down into four phases, which are illustrated in Figure 1.2. The first phase, the downstroke, occurs when the insect rotates its wings about a body-fixed axis from behind its body towards the front. This rotation occurs at a relatively constant angle of attack and angular velocity [3]. At the end of the downstroke, the wing rotation slows and the wings pitch up rapidly; this phase is known as supination. In the upstroke, the wings rotate from the front of the body toward the back, in a manner similar to the downstroke. At the end of the upstroke, in the phase known as pronation,

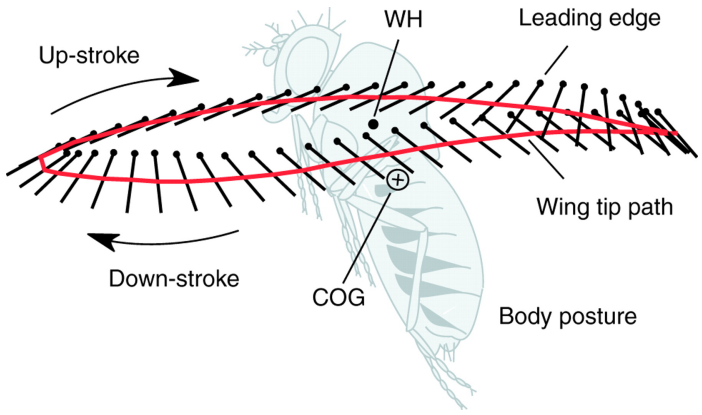

Figure 1.2: *Drosophila melanogaster* wingtip trajectory [6].

the wing rotation again slows and the wing pitches up in preparation for the next downstroke [4]. One parameter for describing the kinematics of a wingstroke is the stroke plane angle. The stroke plane is defined as the plane that best fits the path traced out by the wingtip of the insect over the duration of one wingstroke. A breakdown of the stroke plane angle for a variety of insects can be found in Ref. [4], and includes insects with horizontal, inclined, and vertical stroke planes, corresponding to stroke plane angles of 0 deg, between 0 deg and 90 deg, and 90 deg, respectively. An insect wing stroke can be further parameterized by noting a deviation from the stroke plane as a function of time, which describes the angle of inclination above or below the average stroke plane at a given point in the wingstroke [5].

The four phases of a flapping wingstroke are illustrated in Figure 1.3 by stills taken from a video [7] of a live hovering hawkmoth (*Manduca sexta*), with a stroke plane angle of approximately 23 deg. As seen in this figure, especially during pronation and supination, wing kinematics of live animals are complicated by wing flexi-

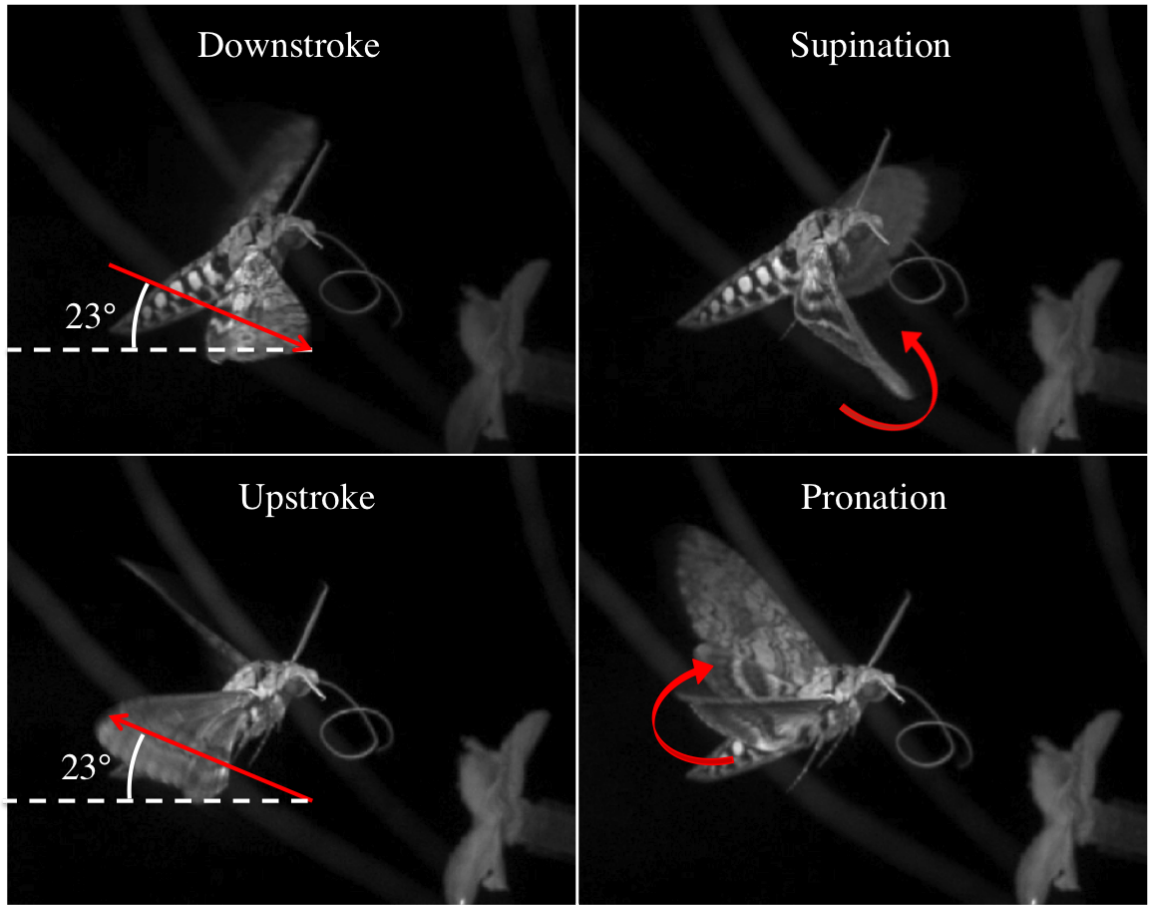

Figure 1.3: Wingstroke phases of *Manduca sexta* [7].

bility.

The complex kinematics of an insect wingstoke have been simplified in various ways for experimentation. In many cases, wing flexibility is ignored and a horizontal stroke plane is assumed for a model of hover. Another common assumption is that the wing tip path is always coincident with the stroke plane. This reduces the flapping kinematics to a combination of rotation and pitching, or the two-dimensional case of translation and pitching. Pure pitching motions have been used to study vortex shedding during pronation and supination [8], while rotating motions [9, 10, 11]

and translating motions [12, 13, 14] have been used to study the downstroke. Combined pitching and plunging [15], pitching and translating [16], and pitching and rotating [17] wings have also been used to simulate flapping kinematics. Experiments on these motions and combinations of motions, have produced a large body of work relevant to low Reynolds number flapping flight.

1.4 Quasi-Steady Analysis

In an attempt to quantify the lift and drag produced by a flapping wing, early investigations employed a quasi-steady assumption: the aerodynamic forces generated by a wing at any point in time are assumed to be equal to the steady state forces generated by the wing at the same velocity and angle of attack. Blade element analysis can be used in conjuction with the quasi-steady assumption to predict forces on a rotating wing. To employ a blade element analysis, each wing is broken down into thin chordwise sections of width dr along the wingspan, as shown in Figure 1.4. For each section, the lift, L' and profile drag D'_{pro} for each section are determined by the equations

$$L' = \frac{1}{2}\rho c U_r^2 C_L, \tag{1.1}$$

$$D'_{pro} = \frac{1}{2}\rho c U_r^2 C_{D,pro}. \tag{1.2}$$

Under the quasi-steady assumption, given the geometry of the wing section, the lift and drag coefficients are functions only of the angle of attack and the local Reynolds number [18]. The total lift and drag generated by a wing is then calculated by summing the contribution to lift and drag from each chordwise slice. For the quasi-

steady assumption stated previously to be valid, the component of the quasi-steady vertical force averaged over one wing stroke must equal the weight of the insect, while the quasi-steady average horizontal force must be zero [19].

In 1972 Weis Fogh determined that for fruit flies and humming birds, both of which have a horizontal stroke plane, the theoretical lift calculated using a quasi-steady analysis was sufficient to maintain hovering flight. Based on this finding, he concluded that "[t]here is therefore no reason to believe that non-steady aerodynamics is involved to any significant extent" [19]. However, in 1984, Ellington, after a reanalysis of historical data, reached the opposite conclusion, that unsteady phenomena were in fact, integral to generating enough lift to keep insects and birds with a horizontal stroke plane aloft in hovering flight [4, 18].

Ellington argued that if the mean lift coefficient satisfying the net force balance (where lift equals weight and thrust equals zero), $\overline{C_L}$, is greater than the maximum lift coefficient derived from the quasi-steady analysis, $C_{L,max}$, then the quasi-steady assumption must be invalid. Based on a limited knowledge of $C_{L,max}$, only two of the insects with horizontal stroke planes Ellington examined, *Encarsia* and *Aeschna*, met this criteria. However, if the values of $\overline{C_L}$ and $C_{L,max}$ are close, it does not prove that the quasi-steady assumption is valid, only that it cannot be ignored. This is because unsteady lift mechanisms, which use changes in wing geometry or configuration to enhance lift above what would be seen in steady flow, could be contributing to the lift and yielding forces that are similar to the quasi-steady forces. Citing the large errors in $C_{L,max}$ calculated independently by Weis-Fogh and Nachtigall, and that unsteady lift coefficients seen in flapping flight may be lower

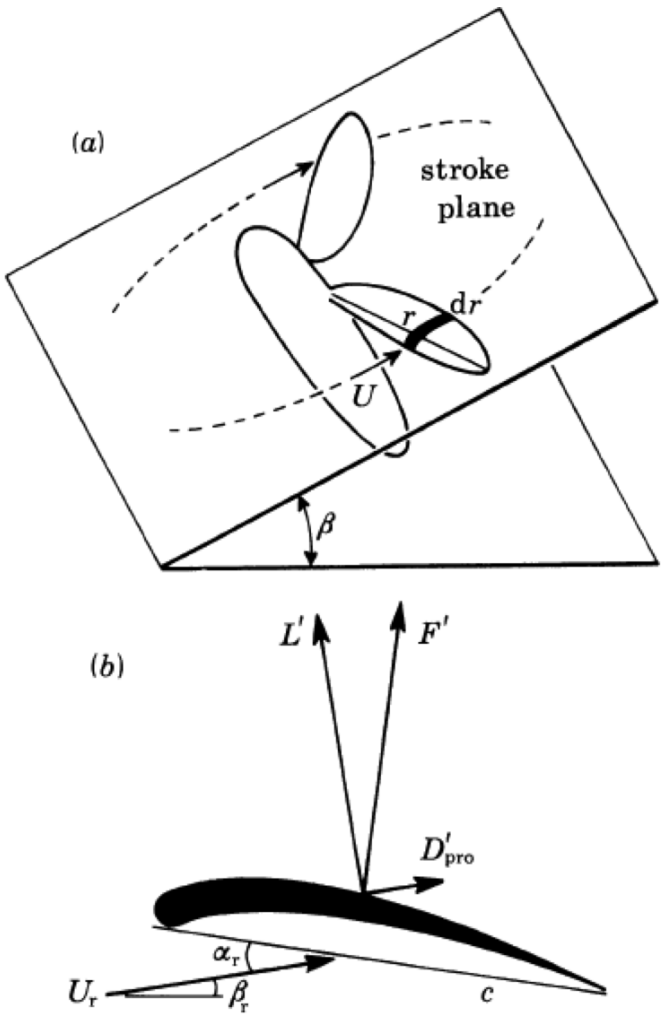

Figure 1.4: Blade element analysis of model flapping wing [4].

than quasi-steady estimates because of the Wagner effect, Ellington concluded that unsteady mechanisms are likely important for most insects and birds with horizontal stroke planes [4]. The invalidity of the quasi-steady assumption was later confirmed by other researchers [20, 21].

Thus, insects and hovering birds do not remain aloft using traditional aerodynamic lift generation mechanisms. Flying at low Reynolds numbers and high angles of attack with relatively short wingstrokes, they must employ unsteady methods of

lift generation. Since the quasi-steady model was discounted, many researchers have begun to investigate the aerodynamics of such mechanisms and their applications to flapping flight [22, 15].

1.5 Unsteady Lift Mechanisms

1.5.1 Wagner Effect

One of the earliest well understood and experimentally confirmed unsteady lift mechanism is the Wagner effect. Assuming pre-stall angles of attack and attached flow, the Wagner effect postulates that in cases where the steady state bound circulation around a wing changes instantaneously, there will be a delayed growth in circulation and lift. Examples of such instances are an impulsive translational motion or an impulsive change in angle of attack. In 1925, Wagner showed that the starting vortex shed from the trailing edge of an impulsively started airfoil induces a downwash on the wing [23]. This downwash lowers the effective angle of attack seen by the airfoil and hence, decreases the lift. As the starting vortex is convected away from the wing, its influence decreases and the lift rises. After six chord-lengths traveled, the lift is approximately 90% of its steady state value. The Wagner function, while known exactly, is not in an analytical form convenient for analysis, and is therefore often approximated. Two common approximations were an exponential model developed by R.T. Jones in 1938 [24] and an algebraic model developed by Garrick in 1938 [25]. The exact Wagner function, representing the ratio of the instantaneous bound circulation to the steady state bound circulation, and these two

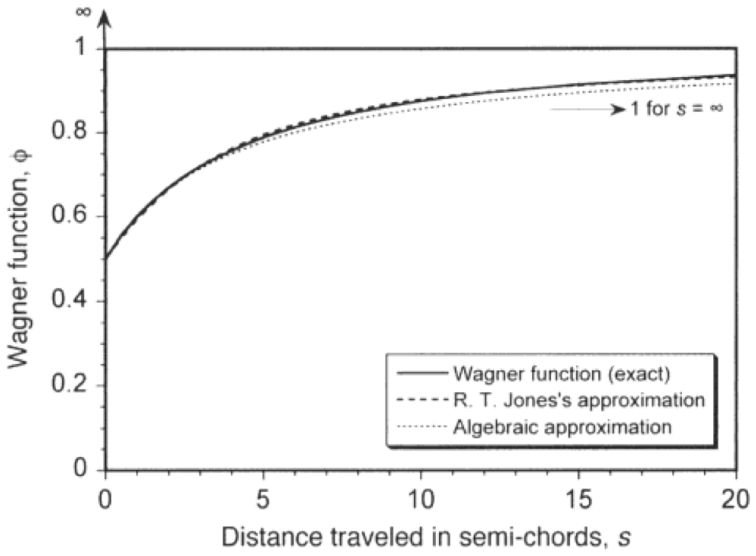

Figure 1.5: Wagner's function [26].

approximations are plotted in Figure 1.5. Because the typical insect wing stroke is short, only two to four chord-lengths traveled at the wing tip [20], the Wagner effect is important, although it acts to diminish lift instead of enhance it.

1.5.2 Delayed/Dynamic Stall

In 1933, Francis and Cohen repeated experiments done by Walker confirming the Wagner effect, except at post stall angles of attack, where the assumptions underlying the Wagner effect are violated [27]. They found that for the first three chord-lengths of travel, the bound circulation of the wing grew at a rate similar to that predicted by the Wagner equation. After three chord-lengths, the circulation stopped growing, an indication of stall. This result is notable because instead of stalling immediately after the wing began moving, the circulation initially grew

to values higher than the stalled circulation value. This phenomenon is know as delayed, or dynamic, stall, in which an airfoil can achieve lift coefficients above steady state value for the first several chord-lengths traveled.

Dynamic stall has also been studied in depth more recently by several researchers. In a 2009 paper by Ol [15], he studied the forces and flow features associated with 2D flat plates in pure plunge and pitch/plunge motions with reduced frequencies (the ratio of wingstroke to freestream velocity) similar to flapping flight cruise for birds. He found that Theodorsen's formula was able to reasonably predict lift coefficients, even in cases of deep stall, where the formula's assumptions of fully attached flow and a planar wake are clearly violated. He also found that below stall, Reynolds numbers ranging from 10,000 to 60,000 affected the size of the laminar separation bubble, but post stall, Reynolds number effects were negligible.

Dynamic stall is characterized by the formation, development and shedding of a leading edge vortex (LEV). As the vortex forms, and after it sheds but is still above the wing surface, the vortex causes a significantly different pressure distribution along the airfoil surface than would be seen in steady flow. The increased low pressure on the top surface of the wing leads to higher lift [28, 15]. As with the Wagner effect, because insects have short stroke amplitudes and start and stop so frequently, delayed stall plays an important role in the development of forces produced by flapping wings.

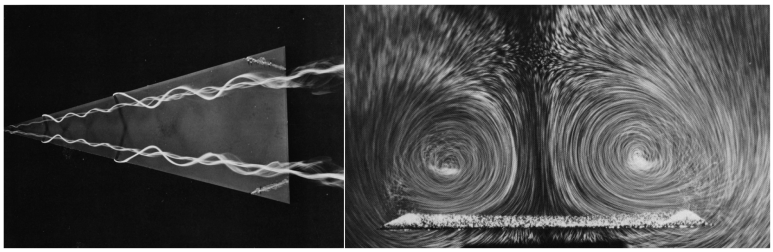

Figure 1.6: Leading edge vortices on a delta wing.[29]

1.5.3 Vortex Lift

The ability of vortices to enhance lift has been studied for applications in delta wing aircraft, including the Concorde [20]. The swept, sharp leading edges of a delta wing at subsonic speeds cause flow separation resulting in a pair of spiraling vortices on the swept leading edges of the top surface of the wing, as seen in the flow visualizations from above (left) and behind (right) a delta wing in Figure 1.6. These vortices reduce the static pressure near the leading edge on the top surface of the wing, significantly enhancing the lifting capability of the aircraft.

Although insect flapping occurs at much lower Reynolds numbers than those in delta wing flight, large vortices were seen in early modeling of insect flight that resulted in similarly enhanced lift. In 1979, Maxworthy used dye flow visualization to capture the large vortices created during the clap and fling mechanism, where the two wings of an insect begin the downstoke clapped together behind the body and peel apart from each other as they rotate toward the front of the body. One of his dye visualizations is shown in Figure 1.7.

Early studies modeling insect flapping found that flow separating over the

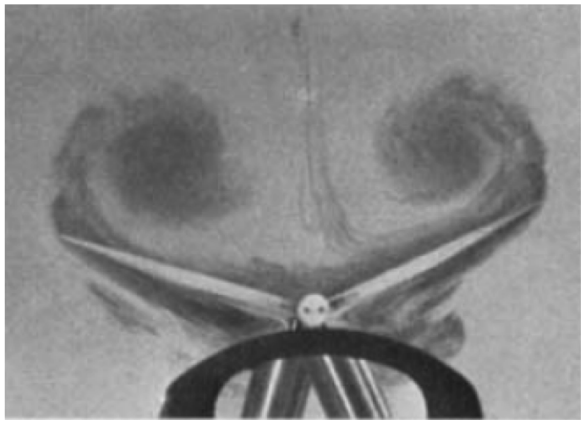

Figure 1.7: Dye flow visualization of LEVs during clap and fling [22].

leading edge of a wing at a high enough angle of attack resulted in the formation of large leading edge vortices, which were fed by vorticity produced at the leading edge of the wing [28, 5]. Because these vortices only enhance lift while they are attached or while they are above the surface of the wing, much effort has been spent on determining how to stabilize them, examples of which are discussed in the following section. In a study of translating plates accelerating from rest, Dickinson observed the presence of an LEV that remained attached for two chord-lengths of travel and was then shed. The corresponding lift data showed that the presence of this vortex resulted in an 80% increase in lift compared to 5 chord-lengths of travel later, after vortex shedding [20]. Subsequently, a study by the same author on rotating plates found that rotating wings are capable of maintaining a stable leading edge vortex for up to 5 chord-lengths of travel, longer than the typical insect wing stroke of 2 to 4 chord-lengths. He postulated that the spanwise flow along the wing helped to stabilize the LEV [30]. If stability can be achieved for only a few chord-lengths of

travel, the stroke-averaged lift coefficient can be significantly increased, due to the relatively short stoke-to-chord ratios of typical insect flight.

1.6 Recent Experiments on Models of Flapping Wings

1.6.1 Summary

Many different models and types of wing kinematics have been used to simulate flapping wing flight, including translating or rotating at fixed angles of attack to model the downstroke. Examples of these types of experiments, in addition to kinematics for modeling other phases of the flapping wingstroke, are given in Section 1.3.

1.6.2 Translating Wings

As mentioned previously, early studies of translating wings as models for the insect downstroke include the work of Dickinson and Götz [20]. They analyzed two-dimensional flat plates rapidly accelerating from rest at fixed angles of attack. They found that for angles of attack above 13.5 deg, a leading edge vortex formed and remained attached to the wing for two chord-lengths of travel. This LEV contributed to an 80% rise in lift when compared to the performance of the same wing 5 chord-lengths later. They also found that the presence of the LEV was accompanied by a trailing edge vortex, which acted to decrease lift production. Dickinson claimed that because fly wings typically travel only 2-4 chord-lengths during one half-stroke, the dynamics of an impulsively started wing better approximate the flow than do

steady wing motions.

Studies on translating wings also included work by Ringuette, who found that the three-dimensional effects introduced by the presence of a tip vortex acted to increase the lift coefficient of a translating wing. Suppressing the tip vortex formation resulted in a decrease in lift. He also found that the drag coefficient was higher at lower aspect ratios [12].

Potential flow models of impulsively started translating flat plate wings have also been developed. Pitt Ford and Babinsky [31] fitted a potential flow model to experimental data from a translating wing and found that the model most closely approximated the experimental results in the absence of bound circulation. This led to the conclusion that post-stall, lift on wings translating at low Reynolds numbers is produced by LEV development and non-circulatory forces as opposed to bound circulation, in support of Dickinson's conclusions 9 years prior.

1.6.3 Rotating Wings

In early rotating wing experiments, Dickinson found that rotating wings are capable of maintaining a stable leading edge vortex for up to 5 chord-lengths of travel, as compared to 2 chord-lengths for translating wings. He postulated that the spanwise flow along the wing helped to stabilize the LEV [30] .

More recent rotating wing experiments include those of Jones and Babinsky [9, 32]. They used particle image velocimetry (PIV) and force measurements to analyze rotating wings at a Reynolds number of 60,000. They found that the presence of

a leading edge vortex caused a peak in lift approximately 1.5 times greater than the quasi-steady state value occurring after 2.4 chord lengths traveled at the three-quarter chord, when subsequent LEVs continue to form and shed.

1.6.4 Limitations of Previous Experiments

Despite the large existing body of research modeling flapping flight, very few rotating wing experiments have examined the flow at rotation past 90 degrees. One example, however, is the work of Kolluru and Jones [33], which examined the flow field and force history of wings rotating up to two revolutions through flow visualization and force measurements. They found that in the second revolution of travel, both lift and drag dropped significantly as compared to the first revolution. However, no comparison was made to the translating data of a similar wing. Additionally, few comparisons have been made between the forces generated by geometrically similar rotating and translating wings. The study by Jones and Babinsky [9] noted above does provide a comparison of force data between rotating and translating wings, but, as this study had a maximum rotation angle of 90 degrees, a comparison at higher rotation angles is still needed. DeVoria and Ringuette have also studied rotating flat plate wings [10], performing dye flow visualization and PIV on trapezoidal wings at a 90 deg angle of attack. They examined the shedding of the initial ring-shaped vortex and the formation of a new vortex attached to the wing. This phenomena, where the vortex has absorbed all of the vorticity from the flow that it can and then separates, is known as vortex saturation. Maximum rotation angles studied in this

experiment were 120 deg, but no force data was collected.

1.6.5 Experiments in Tanks

Many flapping wing experiments have been been performed underwater, in oil, or in glycerin, which have the advantage of slower wing motions for larger wings than experiments in air for Reynolds characteristic of flapping flight. However, due to size restrictions on the tanks used for experimentation, it is necessary to be aware of the maximum size wing that can be tested in a given tank without loss of data accuracy from wall effects. Recent flapping wing experiments involving three-dimensional wing kinematics in enclosed tanks include those by DeVoria et al. [10], Ozen and Rockwell [34], Kolluru and Jones [17], Jones and Babinsky [9], Lentink and Dickinson [11], Kim and Gharib [35], and Wojcik and Buchholtz [36].

DeVoria et al. examined low aspect ratio trapezoidal wings rotating at a fixed angle of attack of 90 degrees for up to 120 degrees of revolution. These experiments were performed for Reynolds numbers $O(10^3)$ in a water tank with dimensions of $210\,\text{cm} \times 91\,\text{cm} \times 71\,\text{cm}$. The wing models used had a maximum spanwise length of 9 cm and a chord length of 9 cm. If placed in the middle of the tank, this yields a minimum distance from the wing tip to a tank wall of 4.1 chord-lengths [10].

Ozen and Rockwell studied flat plate wings at fixed angles of attack between 30 and 75 degrees for Reynolds numbers ranging from 3,600 to 14,500 and rotation angles up to 270 degrees. Their experiments were performed in a free-surface water channel with dimensions of $4{,}877\,\text{mm} \times 927\,\text{mm} \times 610\,\text{mm}$, using wing models with a

chord of 73.9 mm, span of 73.9 mm, and distance from the rotational axis to the wing root of 38.1 mm. These dimensions result in a minimum wing tip-to-wall distance of 4.6 chord-lengths [34].

Kolluru and Jones studied rectangular flat plate wings rotating at fixed and variable angles of attack. Experiments were performed at a Reynolds number of 5,000. The wing used was an aspect ratio 2 plate with a chord length of 3 inches and a distance from the axis of rotation to wing root of 0.65 chord-lengths. This water tank had dimensions of $4\,\text{ft} \times 4\,\text{ft} \times 4\,\text{ft}$. Therefore, the minimum distance from the wing tip to the side wall of the tank was 5.4 chord-lengths [17].

The minimum wingtip-to-wall distance in the experiments by Jones and Babinsky was 2.4 chord-lengths at a Reynolds number of 60,000 for a maximum rotation angle of 85 degrees [9].

Lentink and Dickinson performed experiments on a pair of *Drosophila* wings traveling through a maximum rotation angle of 140 degrees in a reciprocating motion for up to six cycles. The minimum wall distance in this investigation was 1.8 chord-lengths at a Reynolds number of 14,000 [11].

Kim and Gharib examined rotating flat plates at $Re = 60$ and $8,800$ with a maximum rotational angle of 112.5 degrees. The tip clearance on their experiments was 1.1 chord-lengths [35].

Wojcik and Buchholtz also performed experiments on rotating wings using Reynolds numbers between 4,000 and 16,000 for stroke angles up to 320 degrees and had a tip clearance of 9.7 chord-lengths [36].

A summary of the important experimental parameters and the tip clearance

Table 1.1: Summary of tip clearances for recent experiments.

Researchers	Year	Reynolds number	Maximum rotation angle	Tip clearance
Devoria et al. [10]	2011	$O(10^3)$	120 deg	$4.1c$
Ozen and Reockwell [34]	2011	3,600-14,500	270 deg	$4.6c$
Kolluru and Jones [17]	2012	5,000	720 deg	$5.4c$
Jones and Babinsky [9]	2010	60,000	85 deg	$2.4c$
Lentink and Dickinson [11]	2009	14,000	140 deg reciprocating 6 cycles	$1.8c$
Kim and Gharib [35]	2010	60 and 8,800	112.5 deg	$1.1c$
Wojcik and Buchholtz [36]	2012	4,000 - 16,000	320 deg	$9.7c$

for each of these experiments is presented in Table 1.1.

As these examples show, typical tank tests on rotating wings are currently being performed in tanks with a wide range of tip clearance between 1.1 and 9.7 chord-lengths. Testing in air is much less restrictive, since hovering requires no free-stream velocity component and experiments can be performed in a large room instead of a confined space like a wind tunnel or water tank. However, the current trend is to perform experiments in fluids with higher densities and viscosities, e.g., glycerin and glycerin/water mixtures, to better resolve the low aerodynamic forces produced by small-scale flapping wings. Given the difficulty of constructing and maintaining large experimental tanks, it is desirable to increase the size of the wing relative to the tank. Additionally, recent experiments have also attempted to characterize the flow after the initial transient of the wing stroke, requiring multiple

wing strokes that are more likely to induce a secondary flow in a relatively small tank.

1.7 Thesis Summary

1.7.1 Objectives

Many researchers have attempted recently to understand the aerodynamics of low Reynolds number flapping wing flight for applications in MAV development. However, the complicated unsteady lift mechanisms involved are still not fully understood. Previous studies have offered many models of flapping flight to address these issues, but have not been able to fully explain how unsteady lift mechanisms contribute to insect flight.

This study aims to fill some of the gaps left by previous research. The effects of certain parameters on the forces generated by an aspect ratio 2 flat plate inclined at a 45 degree angle of attack in pure rotation were studied. These parameters include maximum rotation angle, acceleration distance, and distance from the axis of rotation to the wing root. Because both rotating and translating wings have been used to study LEV formation, development, and shedding, it would be convenient to have a basis on which to compare the forces produced by such wings. However, it is unclear how rotating wing forces should be normalized for comparison with translating wings. Therefore, two methods of reference plane determination and force non-dimensionalization are examined, the axis-relative method and the root-relative method. Where relevant, the rotating cases studied were compared

to a geometrically similar translating wing in an attempt to establish a basis for comparison of the forces generated.

Additionally, the current work aims to determine whether a 5-chord wing tip-to-wall clearance boundary condition is sufficient to approximate tests performed in infinitely large volumes of fluid, what the minimum required distance is, and how the presence of solid tank walls affects the flow field and forces produced by a wing rotating through two revolutions.

1.7.2 Outline

Chapter 1 has presented an overview of unsteady lift mechanisms inherent to low Reynolds number flapping wing flight. Additionally, a detailed account of previous experiments and their conclusions were given. Chapter 2 will provide an overview of the methods used to examine some of the parameters affecting the forces and flowfields of low Reynolds number rotating wings. An overview of the setup for a computational analysis, flow visuaization, and experimental force data collection is provided. Chapter 3 details the results of the boundary condition analysis conducted computationally and through flow visualization. Chapter 4 discusses the results of the parameter study investigating how maximum rotation angle, acceleration profile, and root cutout effect the aerodynamic forces produced by rotating wings. Also, two methods for reference plane determination and force non-dimensionalization are compared. Force coefficients are also compared to data collected at AFRL for rotating and translating wings. Chapter 5 provides the conclusions of this study,

and discusses avenues for further research.

Chapter 2

Methodology

2.1 Overview

Both computational and experimental techniques were used to evaluate the flow field and forces produced by a rotating wing. Numerical simulations were used to determine the minimum possible size of a tank containing a rotating wing such that the effects of the tank walls on the flow features and forces of the wing are negligible. Numerical simulations also provided an understanding of the flow features (leading edge vortices, wing wake, etc.) inherent to a wing rotating at a low Reynolds number and high angle of attack. With the proper wing/tank sizing determined through numerical simulations, experiments were designed to measure the forces produced by rotating wings as a function of parameters including maximum rotation angle, acceleration profile, and root cutout.

2.2 Boundary Study

2.2.1 Computational Model

Wall effects have long been a concern for low Reynolds number rotating wing experiments, but this can not be addressed experimentally because the baseline case, where no wall boundaries are present, cannot be established experimentally. This

is due to the fact that low Reynolds number experiments such as these are usually performed in water or some other exotic fluid (e.g. glycerin or mineral oil), which must be contained inside a tank. A more viscous fluid allows for the use of larger wings which produce forces that are bigger, and hence, easier to measure, while still maintaining a low Reynolds number. Once the wall effects have been quantified computationally and are well understood, this information can be applied to the design of experiments.

Computational studies were performed using the Immersed Boundary Implicit Navier-Stokes (IBINS) solver developed at the University of Maryland [37]. IBINS performs a direct numerical simulation of the Navier-Stokes equations, advancing in time using a Crank-Nicolson scheme on the viscous terms and a second-order explicit Adams-Bashforth method on the inviscid terms. This solver has been optimized for flapping wing kinematics with Reynolds numbers ranging from 10^2 to 10^4. Additionally, IBINS was validated by Bush et al. both experimentally [38] and through comparison with published results for Reynolds numbers ranging from 10^1 and 10^4. The immersed boundary framework involves a modification to the governing Navier-Stokes equations which takes into account the boundary conditions imposed on the flow by the wing surface: zero penetration of flow into the wing, no slip, and zero pressure gradient normal to the wing surface.

An immersed boundary framework is convenient for flapping wing problems because it uses a cartesian mesh that does not necessarily conform to the wing shape. As the wing moves, the mesh remains fixed. The solver determines which mesh nodes are inside of and outside of the space occupied by the wing and solves the

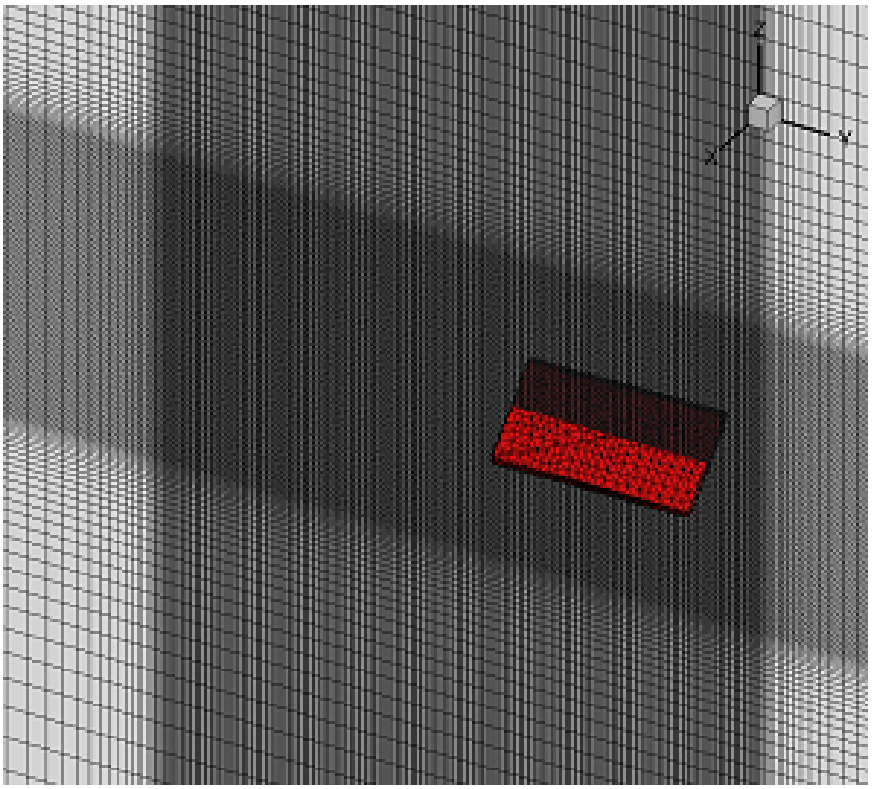

Figure 2.1: Computational wing and fluid mesh.

governing equations accordingly. This eliminates the need to regenerate a new mesh when the wing moves at every time step. A grid resolution study was performed to ensure that the mesh spacing was small enough to provide accurate results, and that decreasing the mesh spacing further would not increase the accuracy. The mesh produced as a result of the grid resolution study has small node spacing, $0.015c$ in the x and y directions and $0.020c$ in the z direction, in the region close to the wing. The region of small node spacing extended $0.8c$ above the leading edge and below the trailing edge of the wing, and $0.5c$ past the wing tip. The mesh was hyperbolically stretched far away from the wing, as shown in Figure 2.1. While the mesh varies in size for the different boundary conditions tested, the part of the fluid mesh that is not hyperbolically stretched remains fixed, and only the hyperbolically stretched region is adjusted depending on the boundary conditions. This allows for good resolution of small-scale flow features close to the wing surface (such as the leading edge vortex) while decreasing the total number of nodes needed (and hence computation time) by decreasing flow resolution far away from the wing, where only larger scale flow structures are expected.

Computations were set up to model experiments, as shown in Figure 2.2, which depicts a view from above of the wing rotating in a tank with a square cross section. In this configuration, the wing begins with its midchord aligned with the x-axis. The aspect ratio 2 wing is placed at a 45 deg angle of attack relative to the xy-plane, and rotates counterclockwise about the z-axis. A wing mount connecting the wing root at the midchord to the rotation axis is shown for clarity, although it is not modeled in the simulations. The distance between the wing root and the axis of rotation,

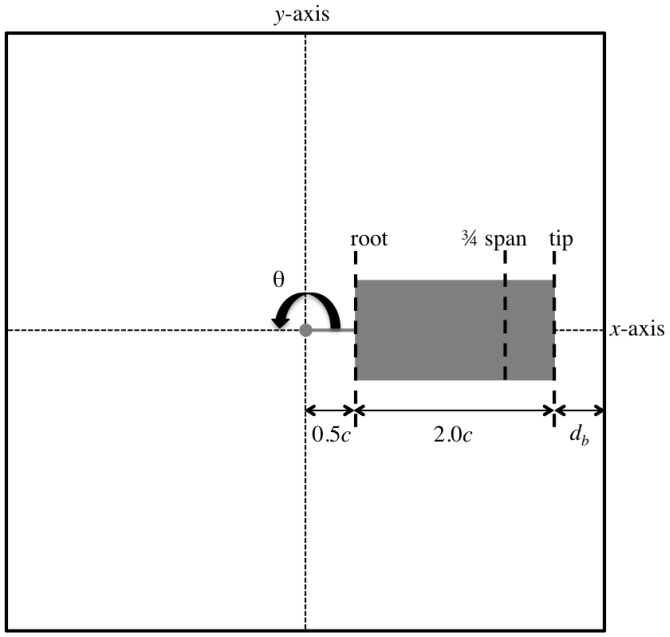

Figure 2.2: Schematic of rotating wing geometry and wall boundaries.

r_r, is fixed at $0.5c$. The boundary conditions on the sides of the mesh parallel to the yz- and xz-planes are set such that they represent solid walls; boundary conditions of no slip, no penetration, and zero pressure gradient are enforced. The variable d_b, representing the tip clearance, or the distance from the wing tip to the wall boundary, is varied from $0.5c$ to $5.0c$. The infinite case, simulating a wing rotating in an infinitely large volume of fluid, uses boundary conditions of zero pressure gradient and zero velocity gradient at the mesh boundaries. The top and bottom surfaces of the mesh, parallel to the wing rotation plane, are held constant at a distance of $12.5c$ away from the wing rotation plane, regardless of the case. These boundaries, where zero pressure and velocity gradients are enforced, simulate infinite boundaries, where the fluid extends forever above and below the rotation plane of the wing. Thus, the mesh simulates an infinitely tall cylinder of fluid

Table 2.1: Boundary conditions for computational mesh.

Case	X and Y Directions			Z Direction		
	Domain	Pressure boundary condition	Velocity boundary condition	Domain	Pressure boundary condition	Velocity boundary
$d_b = \infty$	$25c$	$\Delta p = 0$	$\Delta v = 0$	$25c$	$\Delta p = 0$	$\Delta v = 0$
$d_b = 5.0c$	$15c$	$\Delta p = 0$	$v = 0$	$25c$	$\Delta p = 0$	$\Delta v = 0$
$d_b = 3.0c$	$11c$	$\Delta p = 0$	$v = 0$	$25c$	$\Delta p = 0$	$\Delta v = 0$
$d_b = 0.5c$	$6c$	$\Delta p = 0$	$v = 0$	$25c$	$\Delta p = 0$	$\Delta v = 0$

with a square cross-section. The assumption that $12.5c$ above and below the wing leading edge is far enough away to simulate infinite boundaries for at least two revolutions (the maximum rotation angle examined in this study) is supported by experimental flow visualization discussed in Chapter 3. The boundary conditions used for computations are summarized in Table 2.1. In this table, mesh size refers to the distance in chord lengths, from one side of the mesh to the other in the given direction, with the axis of rotation in the middle of the xy-plane.

2.2.2 Wing Kinematics

In all of the numerical simulations performed for this work, the wing was accelerated over a distance of $0.17c$ traveled at the wing tip, or $0.13c$ at the three-quarter span (i.e., 75% of the distance from wing root to wing tip), as shown in Figure 2.2. A modified Eldredge smoothing function [8] was used to create a velocity profile where the wing begins at rest, accelerates constantly over a given distance to a set maximum angular velocity, and then maintains a constant velocity. The

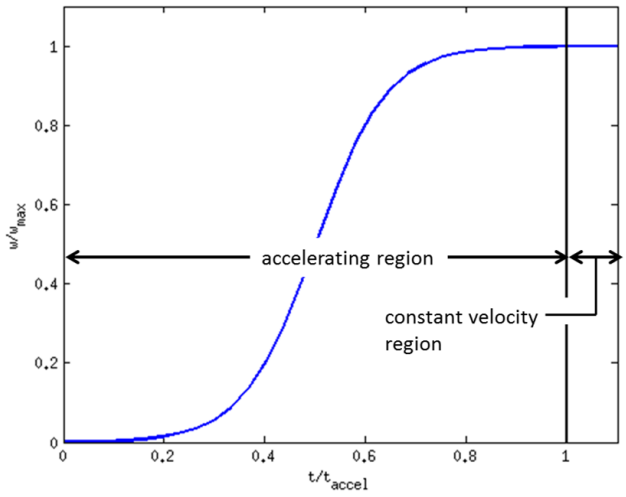

Figure 2.3: Normalized wing velocity profile for computational analysis.

angular velocity profile takes the form

$$\Omega(t) = \frac{k}{a} \log\left(\frac{\cosh(a(t-t_1))}{\cosh(a(t-t_2))}\right) + \frac{\Omega_{max}}{2}. \tag{2.1}$$

In this equation, Ω_{max}, the maximum angular velocity, is set to maintain a local Reynolds number of 120 at the wing tip. This equation results in a velocity profile that is smoothed at the beginning and end of wing acceleration such that there are no discontinuities in the acceleration profile. Although not important for computational testing, smoothing minimizes wing vibration due to fast changes in acceleration in experiments. Because this computational study is intended to model experiments, a velocity profile that would be used for experimental testing was used here, and hence, velocity profile smoothing was included. The amount of smoothing present is controlled by the variable a, which can range from 1 to 100. A small a value corresponds to a minimal amount of smoothing, and a high value of a results in a

heavily smoothed velocity profile. A value of $a = 20$ was used for all computational models. The time constants in this equation, t_1 and t_2 correspond to the instant in time where wing acceleration would begin and end if the velocity profile was unsmoothed. Smoothing results in a non-zero acceleration before t_1 and after t_2. The variable k is the maximum angular acceleration, given by $k = \frac{\Omega_{max}}{2(t_2 - t_1)}$. All cases were run for a maximum rotation angle of 720 deg, at which point the simulation was terminated without bringing the wing to rest. A sample velocity profile is shown in Figure 2.3.

2.2.3 Flow Visualization

Flow visualization was performed using a double-pulsed Nd:YLF laser (Litron LDY304, 30 mJ/pulse,10 kHz max) to illuminate 12 micron silver coated glass microspheres in an 18 in x 18 in x 18 in tank. A schematic of the setup is shown in Figure 2.4. The wing was mounted at the midchord and inclined at a 45 degree angle of attack. Vertical slices (parallel to the xz-plane) of the entire tank were visualized, and illuminated by the laser from the side. All images shown were taken when the wing was positioned as shown in the figure, at whole revolutions. The laser sheet was oriented such that it illuminated the tank cross-section just behind the trailing edge of the wing when the wing mid-span was aligned with the x-axis.

Three rectangular, carbon fiber, aspect ratio 2 wings with chords of 1.2 in, 1.64 in, and 3.00 in were used to achieve tip clearances of $5.0c$, $3.0c$, and $0.5c$ respectively. All cases had a $0.5c$ root cutout and were performed at a tip Reynolds number

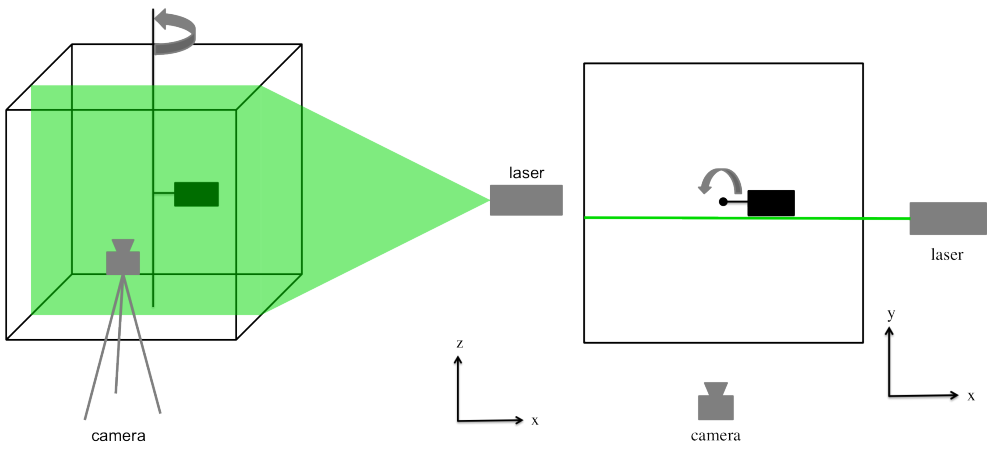

(a) Three dimensional view (b) Top view

Figure 2.4: Flow visualization setup.

of 120. To achieve such a low Reynolds number, the tank was filled with glycerin having a kinematic viscosity of $\nu = 600\,\mathrm{mm}^2/\mathrm{s}$ and a density of $\rho = 1.26\,\mathrm{kg/m}^3$. The same velocity profile as the computational investigation was used, except the wings were allowed to rotate for 45 revolutions before stopping. A Nikon camera was used to take video of the rotating wing at 30 frames per second, and stills were extracted from the video for analysis.

2.3 Aerodynamic Forces Study

2.3.1 Rotating Wing Setup

All rotating wing experiments were performed in an 18 in x 18 in x 18 in tank at the University of Maryland, shown in Figure 2.5. The tank, simpler than a water tunnel, is ideal for simulating hovering kinematics and can be filled with

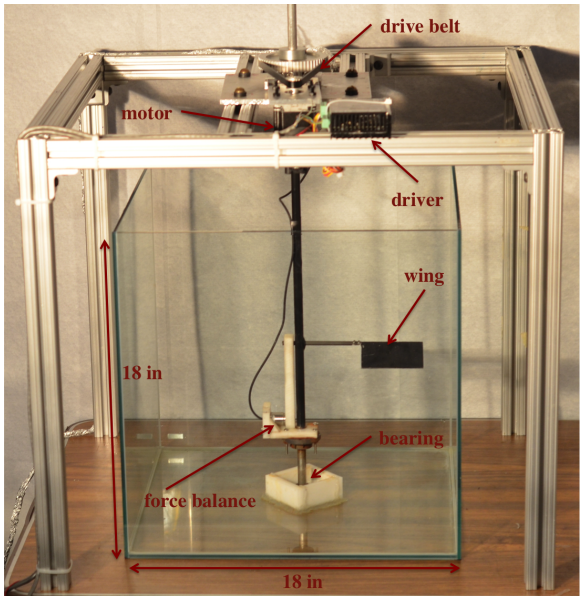

Figure 2.5: 18 in water tank at University of Maryland.

either water or a more viscous fluid such as glycerin, depending on the desired Reynolds number. The wing was rotated about a vertical 0.5 in diameter stainless steel driveshaft rotating in a bearing affixed to the center of the floor of the tank. The shaft was driven by a gear and belt system with a 6:1 gear ratio attached to an Omega OMHT stepper motor and controlled by an Omega STR4 motor driver. The driver takes as input a digital pulse train to drive the motor. Every rising edge, or switch from a zero to a one, is translated into one pulse, rotating the motor a fraction of a degree. The resolution of the motor was set to 12,800 pulses per revolution. The angular velocity of the motor is proportional to the speed at which ones and zeros are fed to the motor driver.

The wing was attached to a mount aligned with the leading edge of the wing and passing through the rotational shaft. The mount was secured to one end of

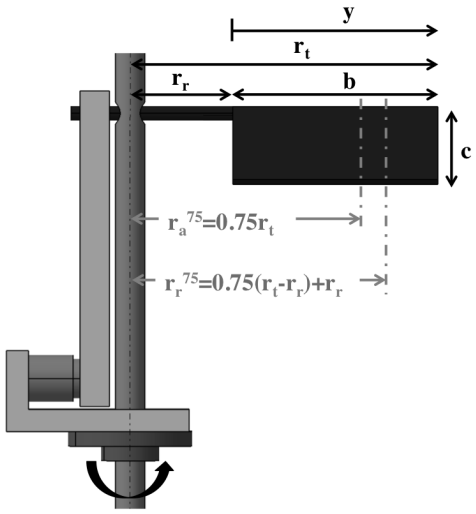

Figure 2.6: Rotating wing geometry.

a vertical strut, which was attached at the other end to an ATI Nano-25 IP68 submersible force/torque sensor. This setup, seen in Figures 2.5 and 2.6, has several distinct advantages. By placing the force balance on the opposite side of the rotation axis from the wing, very small root cutouts, where the wing root comes very close to the rotation axis, can be examined. Additionally, in this configuration, the force balance is three chord-lengths below the rotation plane of the wing, so the wake created by the force balance does not affect the flow field seen by the wing. All wings used were aspect ratio 2 flat plate rectangular wings machined out of aluminum with a 4.0% thickness-to-chord ratio. Each wing had a chord of 1.74 in and sharp edges and corners.

2.3.2 Reynolds Number Calculation and Force Normalization

Because velocity varies along the wing span for rotating wings and geometry varies widely between setups, it is not obvious how to best non-dimensionalize forces over a range of setups, and especially to compare rotational motions to rectilinear ones. The spanwise velocity gradient seen by a rotating wing necessitates the definition of a reference plane for determining a reference Reynolds number and non-dimensionalizing lift and drag forces. Here, two such methods will be examined. The equations defining the reference plane for each method are included in Figure 2.6. The first method, referred to as the *axis-relative method*, defines the reference plane as 75% of the distance from the axis of rotation to the wing tip, r^a_{75}. The second method, the *root-relative method*, defines the reference plane as 75% of the distance from the wing root to the wing tip, , r^r_{75}. These two different methods for determining the location of the reference plane will yield the same result if the root cutout, r_r, is zero. However, as root cutout is increased, the root-relative reference plane will remain at a fixed spanwise location y/b (where b is the wing span and y is the distance from the root of the wing), whereas the axis-relative reference plane will move inboard along the wing as r_r increases. Having defined a reference plane, a reference Reynolds number is defined as

$$Re = \frac{V_{\text{ref,max}} c}{\nu}, \tag{2.2}$$

where

$$V_{\text{ref,max}} = \begin{cases} \Omega_{\max} r^a_{75}, & \text{axis-relative method} \\ \Omega_{\max} r^r_{75}, & \text{root-relative method.} \end{cases}$$

In these equations, c is the wing chord length, ν is the kinematic viscosity, and $V_{\text{ref,max}}$ is the maximum angular velocity at the reference plane.

These two methods also take different approaches for normalizing the aerodynamic forces produced by a rotating wing. The axis-relative method defines the force coefficients $C_F = \{C_L, C_D\}$ as

$$C_F = \frac{F}{\frac{1}{2}\rho V_{\text{ref,max}}^2 cb}. \tag{2.3}$$

This is the standard definition for lift and drag coefficients of translating wings, where the reference velocity is the freestream velocity seen by the wing. Instead of using the velocity at the reference plane for force normalization, the root-relative method assumes constant sectional force coefficients along the wing span. Under this assumption, equations for the force coefficients can be found by integrating the forces along the wing span, i.e.

$$F = \int_{r_\text{r}}^{r_\text{t}} \frac{1}{2}\,\rho\, c\, C_f\, (\Omega_{\text{max}} r)^2\, \mathrm{d}r. \tag{2.4}$$

When the integration is carried out, this yields

$$C_F = \frac{6F}{\rho\, \Omega_{\text{max}}^2 c\, (r_\text{t}^3 - r_\text{r}^3)}. \tag{2.5}$$

The rotating kinematics were defined such that the axis-relative Reynolds number was maintained at 10,000 for all root cutouts. The spanwise velocity distribution along the wing span for two of the root cutouts tested, $0.5c$ and $2.5c$, is illustrated in Figure 2.7. Here, the local velocity along the wing span for a root cutout of 0.50 chords and 2.50 chords is compared, and the location of the reference plane according to the axis-relative (solid black line) and root-relative (dashed gray line) methods

is given. Because the wing kinematics were defined according to the axis-relative method, the velocity at this reference plane is the same regardless of root cutout. However, the local velocity at the root-relative reference plane is larger for larger root cutouts. For example, for the $0.50c$ root-cutout case, the local velocity at the root is 0.060 m/s, at the axis-relative reference plane is 0.226 m/s, at the root-relative reference plane is 0.241 m/s, and at the tip is 0.302 m/s. When the root cutout is increased to $2.50c$, the local velocity at the tip and the axis-relative reference plane remain the same, but the root velocity is 0.168 m/s, an increase of 180% from the $0.5c$ case, and the local velocity at the root-relative reference plane is 0.268 m/s, an increase of 11% from the $0.5c$ case. As a result, reference Reynolds number varies with root cutout when using the root-relative method, but the variations are small (on the order of 1,000).

The local Reynolds number distribution along the span can also be examined, and is shown in Figure 2.8. In this figure, a normalized span location of 0 corresponds to the wing root, and a normalized span location of 1 corresponds to the wing tip. The colored lines represent the local Reynolds number distribution along the span for the range of root cutouts investigated. The vertical dotted black lines show the location of the reference plane for each root cutout. The intersection of each vertical dotted black line and the corresponding colored line indicates the reference Reynolds number, marked by a horizontal dotted black line. Figure 2.8(a) shows that although the reference plane moves towards the wing root as the root cutout increases, the reference Reynolds number remains 10,000. The velocity profiles were defined such that this was the case. When the same Reynolds number distributions

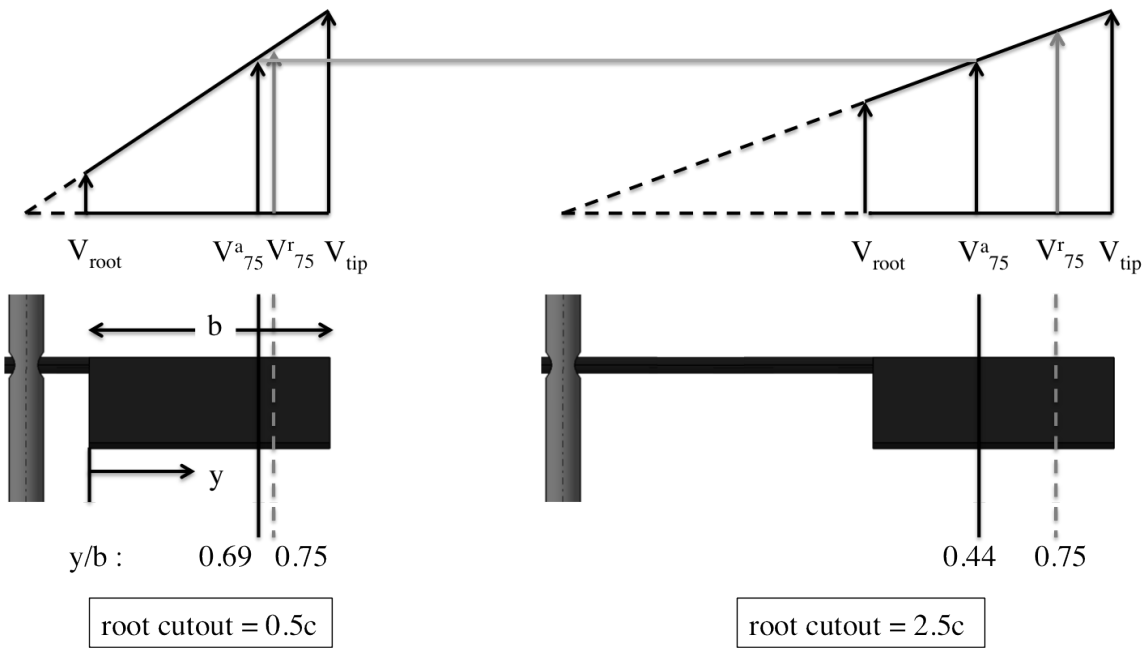

Figure 2.7: Comparison of spanwise local velocity for root cutouts of $0.50c$ and $2.50c$.

are examined from a root-relative perspective, as in Figure 2.8(b), it is evident that although the reference plane remains at a fixed distance along the span, the reference Reynolds number varies slightly, from a minimum of 10,370 at a root cutout of $0.25c$ to a maximum of 11,852 at a root cutout of $2.50c$. Despite the small variation in Reynolds number when defined using the root-relative reference plane, Reynolds number effects in this range are small, and the force coefficients are expected to be very similar [15].

2.3.3 Wing Kinematics

As in the numerical simulations, a modified Eldredge function [8] was used to create the angular velocity profiles for the rotating wing experiments. These

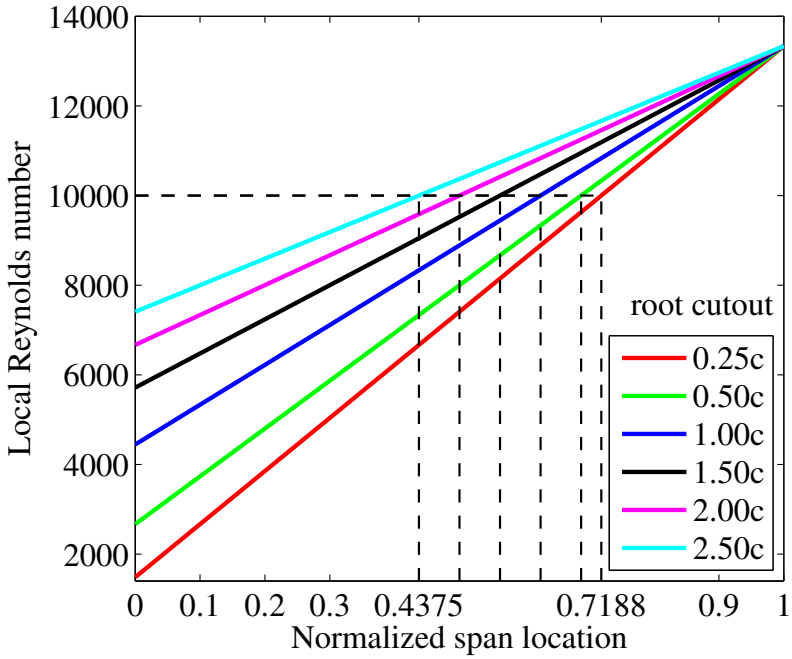

(a) Axis-relative method

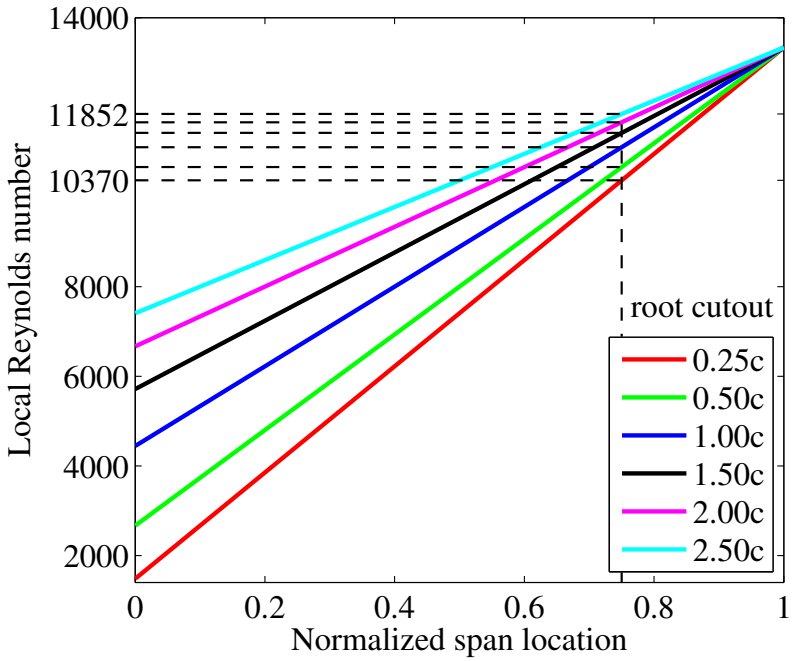

(b) Root-relative method

Figure 2.8: Local Reynolds number along the wing span for $r_r = 0.25c$, $0.50c$, $1.00c$, $1.50c$, $2.00c$, and $2.50c$.

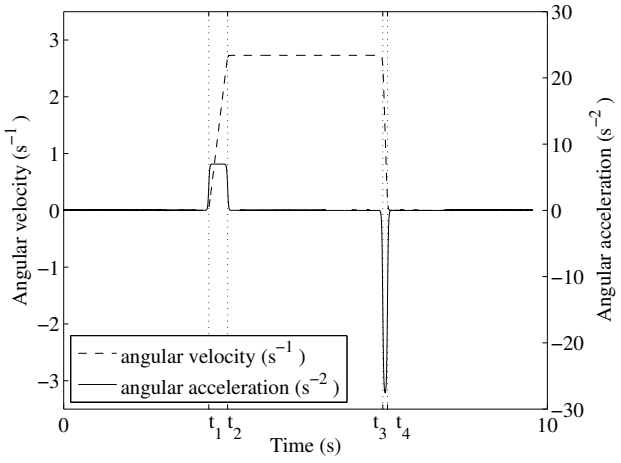

Figure 2.9: Sample velocity profile.

equations take the form

$$\Omega(t) = \begin{cases} \frac{\Omega_{\max}}{2a(t_2-t_1)} \log\left(\frac{\cosh(a(t-t_1))}{\cosh(a(t-t_2))}\right) + \frac{\Omega_{\max}}{2}, & 0 \le t \le \frac{(t_2+t_3)}{2} \\ \\ \frac{-\Omega_{\max}}{2a(t_4-t_3)} \log\left(\frac{\cosh(a(t-t_3))}{\cosh(a(t-t_4))}\right) + \frac{\Omega_{\max}}{2}, & \frac{(t_2+t_3)}{2} < t. \end{cases} \tag{2.6}$$

This angular velocity profile corresponds to a wing that starts at rest, accelerates constantly over a specified azimuthal angle, and maintains a constant velocity thereafter. When the wing approaches the end of rotation, it decelerates over a specified rotation angle. The times corresponding to the beginning and end of wing acceleration are given by the parameters t_1 and t_2, and the times corresponding to the beginning and end of wing deceleration are given by t_3 and t_4. In the angular velocity profile equations, the beginning and end of acceleration and deceleration are smoothed using the smoothing parameter a (see Section 2.2.2). A sample angular velocity profile with respect to time is given in Figure 2.9, with a smoothing parameter of $a = 50$. This value for the smoothing parameter was used for all velocity

profiles for the aerodynamic force analysis. Although the boundary analysis was performed with a smoothing parameter of $a = 20$, it was increased to $a = 50$ for the aerodynamic forces analysis to further decrease the effects of rig vibration on the resultant forces.

2.3.4 Parameter Space

Several parameters, including root cutout, acceleration distance, and maximum rotation angle, were varied to examine their effects on the lift and drag generated by a wing rotating at an axis-relative reference Reynolds number of 10,000. Table 2.2 shows which combinations of root cutout and angular acceleration were tested, all for a maximum rotation angle of 540 deg. Additionally, the baseline case, with a root cutout of $0.50c$ and accelerating over $1.00c$ was examined for maximum rotation angles of 90, 180, 270, 360, 540, and 720 deg. All of these tests were performed in water.

Although insects are not capable of wing rotations greater than 180 degrees, examining rotation angles up to two revolutions allows for examination of wing-wake interaction, a feature inherent to flapping wing flight, with very simple wing motion of rotation in a single direction. In this manner, pitch and modification of rotation direction are avoided.

Table 2.2: Parameter space for maximum rotation angle of 540 deg.

	Acceleration Distance (chords)				
Root Cutout (chords)	0.25	0.50	1.00	2.00	6.00
0.25			X		
0.50	X	X	X	X	X
1.00			X		
1.50			X		
2.00			X		
2.50			X		

2.3.5 Data Analysis

To ensure repeatability, 18 runs were performed for each case. The voltage output from the force balance was converted into three forces and three moments in the direction of the axes of a reference frame centered at the connection between the force balance and the vertical strut. This reference frame was oriented such that the z-axis was aligned with the spanwise direction of the wing and the lift and drag were related to the x and y directions by the equations

$$L = F_x \cos(30^\circ) + F_y \sin(30^\circ) D = F_x \sin(30^\circ) + F_y \cos(30^\circ)$$

where F_x and F_y are the forces in the x and y directions. These transformations from forces in the x- and y-directions to lift and drag are necessary because the force balance reference frame is rotated 30 degrees with respect to the aerodynamic forces reference frame.

The force balance was calibrated by ATI and voltage outputs were converted to forces via a calibration matrix. These forces were transposed into forces in the lift and drag directions. A 4th order lowpass Butterworth filter was applied to

eliminate electrical noise and other sources of high frequency noise above 50 Hz. The natural frequency for each wing configuration was determined by tapping the wing and performing a frequency analysis on the resulting force history while the wing vibrated in response to the tap. 20 Hz bands surrounding the natural frequency of the wing and its higher harmonics were filtered out using 4th order Butterworth bandstop filters, and a 0.08 second moving average, corresponding to $\Delta\theta = 12.5\,\text{deg}$ ($s/c = 0.44$ for $r_r = 0.50$) was applied to each run to further smooth the lift and drag histories.

Vibration in the rig created an additional force in the drag direction, which was eliminated by repeating the 18 runs in water with the wing detached. These runs were averaged and subtracted from the averaged and filtered runs in water with the wing attached. To separate the inertial forces from the aerodynamic forces, 18 runs for each case were also performed in air. Each of these runs was filtered similarly to the runs in water and the 18 runs were averaged together. Runs were also performed in air with the wing detached, and were subtracted for the runs in air with the wing attached. The averaged data taken in air was then subtracted from the averaged data taken in water.

The data at each stage of processing is shown in Figure 2.10. Figure 2.10(a) shows sample lift data taken in water in its raw state, after the 50 Hz lowpass filter was applied, and after the natural frequency bandstop filter was applied. Figure 2.10(b) shows sample lift data after the natural frequency bandstop filter was applied, after the moving average was applied, and after the 20 runs were averaged and inertial forces were removed. Error bars were computed by determining a range

above and below the final lift and drag data into which 95% of the data points from each individual run fell.

2.4 Summary

Computational analysis, flow visualization, and force collection on rotating wings were performed. A computational analysis using IBINS, an immersed boundary implicit Navier-Stokes solver developed at the University of Maryland by Bush [38] was conducted to analyze the effects of wall boundaries on the flowfield and aerodynamic forces of a rotating wing. For this analysis, a rotating wing with a tip Reynolds number of 120 was used. Particle/laser flow visualization was also performed to visualize large scale flow structures in a tank containing a rotating wing, and to establish the effect of the top and bottom surfaces of the tank on the flowfield. The effects of parameters including maximum rotation angle, acceleration distance, and root cutout on the lift and drag produced by a rotating wing were analyzed experimentally at a Reynolds number of 10,000 at the axis-relative reference plane. Two methods for reference plane determination and force non-dimensionalization (the axis-relative and root-relative methods) were examined.

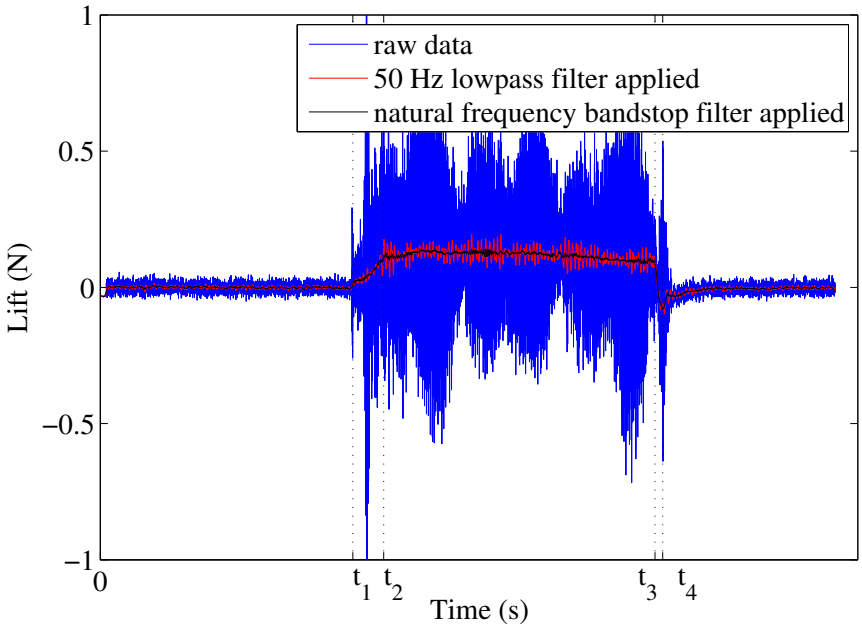

(a) Before averaging runs

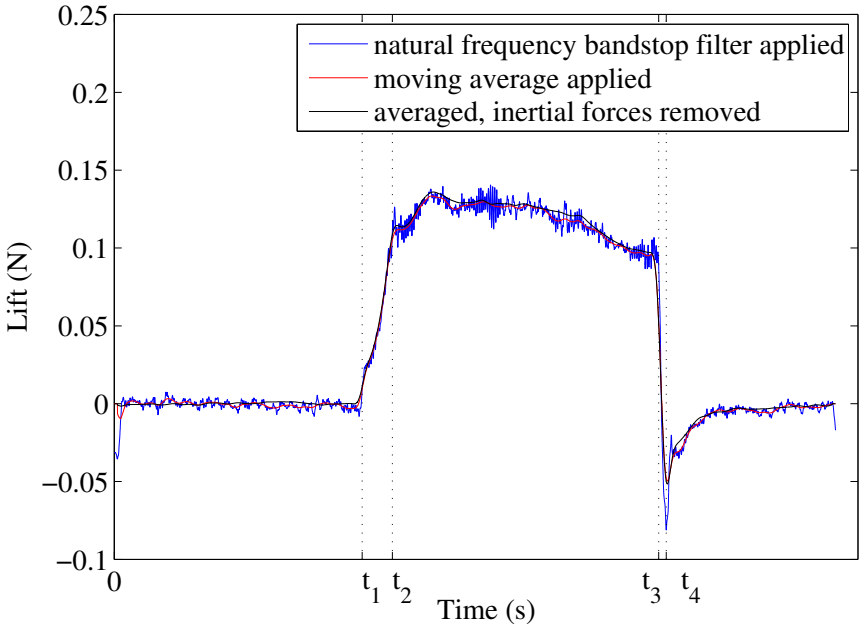

(b) After averaging runs

Figure 2.10: Stages of data processing.

Chapter 3

Boundary Study Analysis

3.1 Overview

A computational analysis was performed to compare the flow structures of a wing rotating in an enclosed space, and the forces produced by such a wing. Four different tip clearances, d_b, as illustrated in Figure 2.2, were analyzed: d_b =0.5c, 3.0c, 5.0c, and the case where d_b approaches ∞, for a tip Reynolds number of 120. This study was performed to provide an idea of the extent to which the tank walls can influence experimental results.

3.2 Data Collection and Visualization

IBINS used the Navier-Stokes equations to calculate the pressure and velocity in all three coordinate directions at every mesh point at every time step. However, the pressure and velocity vectors at every grid point were only recorded approximately every 10 degrees of rotation, or 150 time steps, due to constraints on the space available for data storage. The velocity data stored was also used to calculate Q, a vortex detection parameter, at every mesh point. In order to clearly visualize the flow features, slices of data were taken through the three dimensional mesh space. Flow field slices were taken in both the chordwise and spanwise directions.

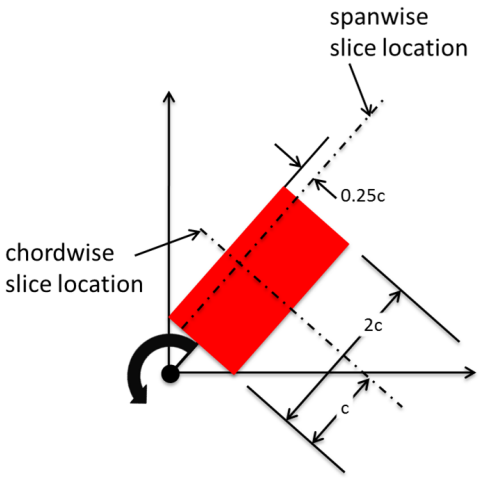

Figure 3.1: Schematic of data plane locations.

Each spanwise cut shown was taken at the quarter chord location, looking from the trailing edge toward the leading edge, with the wing root on the left of the image and the wing tip on the right. Chordwise slices were located at the half span, looking from the wing tip toward the wing root, with the leading edge on the upper right and the trailing edge on the lower left. The locations of spanwise and chordwise slices are illustrated in in Figure 3.1. Some horizontal slices directly above the leading edge of the wing were also taken, with the wing rotating counterclockwise about the rotation axis in the center of each figure. Lift and drag forces integrated over the wing surface and computed from the pressure field were recorded at every time step, or approximately every 0.10 deg.

3.3 Flow Structure

Previous studies of rotating wings with Reynolds numbers $O(10^2 - 10^4)$ have indicated the presence of several dominant flow features. Most notable are the presence of a stable leading edge vortex and spanwise flow from wing root to wing tip [39, 40, 10, 17]. Also present are a strong tip vortex [40, 10, 17] and a starting vortex shed from the trailing edge [10]. These are the flow features expected to be seen in this computational study.

In order to examine the dominant flow structures, chordwise slices were taken of the Q vortex detection parameter at five rotational angles in the first two revolutions, as illustrated in Figure 3.2 . The Q-criterion is a method of vortex determination, and is defined in tensor notation as

$$Q = \frac{1}{2}(u_{i,j}^2 - u_{i,j}u_{j,i}) = -\frac{1}{2}u_{i,j}u_{j,i} = \frac{1}{2}(||\mathbf{\Omega}||^2 - ||\mathbf{S}||^2) > 0, \tag{3.1}$$

where $\mathbf{u}$ is the velocity vector, $\mathbf{\Omega}$ is the vorticity tensor, and $\mathbf{S}$ is the strain rate tensor. Thus, if the Q-criterion holds at a given point (if $Q > 0$), the norm of the vorticity tensor is greater than that of the strain rate tensor, and the point is part of a vortex [41]. Anywhere that $Q \leq 0$ is not part of a vortex. In Figure 3.2, the left column corresponds to the five chord boundary case (the case where $d_b = 5.0c$) and the right column corresponds to the half chord boundary case (the case where $d_b = 0.5c$). In each image, the wing is represented by a solid black line, with the leading edge in the top right of the figure and the trailing edge in the bottom left. The wing is moving from left to right.

After 30 deg of rotation, two large distinct regions satisfying the Q-criterion

and several small regions satisfying the Q-criterion are present for both boundary cases. Near the leading edge on the upper surface of the wing, a large vortex (in red) is present. This region is know as the leading edge vortex (LEV) and is fed by vorticity produced at the leading edge of the wing as it rotates. This LEV remains attached to the leading edge of the wing at all rotation angles shown, although a slight decrease in size is noticeable between 180 deg and 420 deg. An attached LEV that decreases in size between 180 deg and 420 deg is evident for both the $5.0c$ and $0.5c$ boundary cases shown, as well as for the $3.0c$ and infinite boundary cases, which are not shown here. The second distinct region of high vorticity noticeable after 30 deg of rotation is the clockwise oriented vorticity (in red) located just below and behind the trailing edge of the wing. This is the trailing edge vortex (TEV), which is produced when the wing begins to move and shed soon thereafter. By 90 deg of rotation, the TEV has convected out of the frame of the image for both boundary cases and no new TEVs are visible throughout the first two revolutions. The patten of small vortices along the top and bottom surfaces of the wing evident after 30 deg of rotation is non-physical, and is an artifact of the immersed boundary framework. Because the fluid mesh does not conform to the surface of the wing as it rotates, mesh points near the surface of the wing are adjacent to mesh points that are inside the wing and have a non-physical fluid velocity. When the vorticity at a point near the wing surface is calculated, the velocity from the adjacent points inside the wing are considered, yielding false vorticity values for those points. These artificial vortices are present throughout the two revolutions shown and for both boundary conditions, although the exact size and pattern of the small vortices varies as the

wing rotates.

In order to understand how the flow changes from one span location to another, Q contours along a spanwise cut through the wing quarter chord were taken. Figure 3.3 shows these slices for the $5.0c$ and $0.5c$ cases at five rotation angles in the first two revolutions. In this figure the wing, shown in black, is rotating into the page. The wing root is on the left and the wing tip is on the right.

Three distinct vortices are present for all four boundary conditions, including the $3.0c$ and infinite cases, which are not shown, and at all rotation angles. Along the top surface of the wing, the LEV is visible. After 30 deg of rotation, the LEV covers the outboard 3/4 of the wing span. As the wing continues to rotate, the LEV moves away from the wing tip and toward the wing root. Additionally, as in Figure 3.3, a decrease in the size of the LEV is noticeable between 180 deg and 420 deg. The second vortex is concentrated above the wing tip, on the right side of each image. For both boundary cases shown, after 30 deg of travel, the tip vortex appears connected to the LEV. By 90 deg, the tip vortex and the LEV have separated, as the LEV has moved inboard. The third vortex noticeable in these images is the root vortex, on the left side of each image. By 30 deg, the root vortex has reached a size and location that remains constant throughout the two revolutions shown. As seen in the chordwise cuts of Figure 3.3, the pattern of small vortices is visible along the top and bottom surfaces of the wing. As stated previously, this patten is non-physical and an artifact of the immersed boundary framework.

Both Figure 3.2 and Figure 3.3 show a distinct decrease in the size of the LEV between the first revolution and the second revolution, due to downwash from

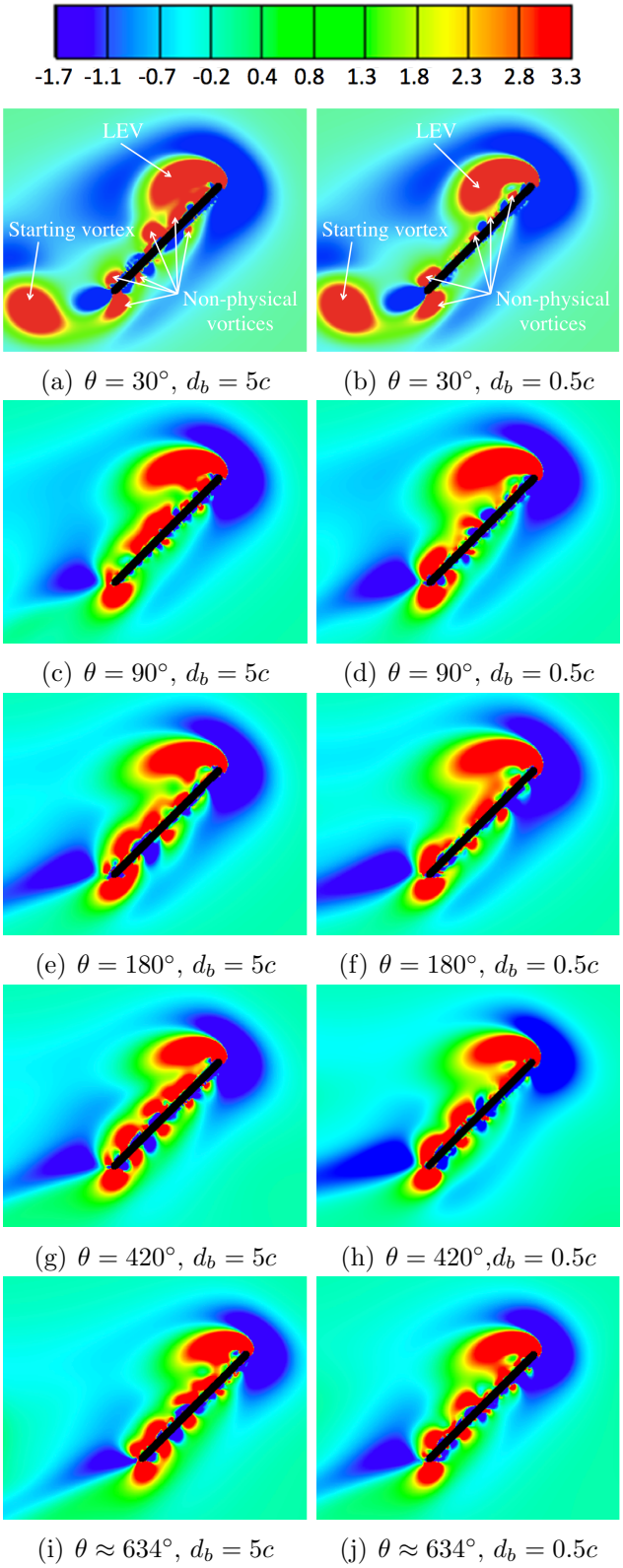

(a) $\theta = 30°$, $d_b = 5c$ (b) $\theta = 30°$, $d_b = 0.5c$

(c) $\theta = 90°$, $d_b = 5c$ (d) $\theta = 90°$, $d_b = 0.5c$

(e) $\theta = 180°$, $d_b = 5c$ (f) $\theta = 180°$, $d_b = 0.5c$

(g) $\theta = 420°$, $d_b = 5c$ (h) $\theta = 420°$,$d_b = 0.5c$

(i) $\theta \approx 634°$, $d_b = 5c$ (j) $\theta \approx 634°$, $d_b = 0.5c$

Figure 3.2: Chordwise views of Q at half-span for the $5.0c$ (left) and $0.5c$ (right) boundary conditions.

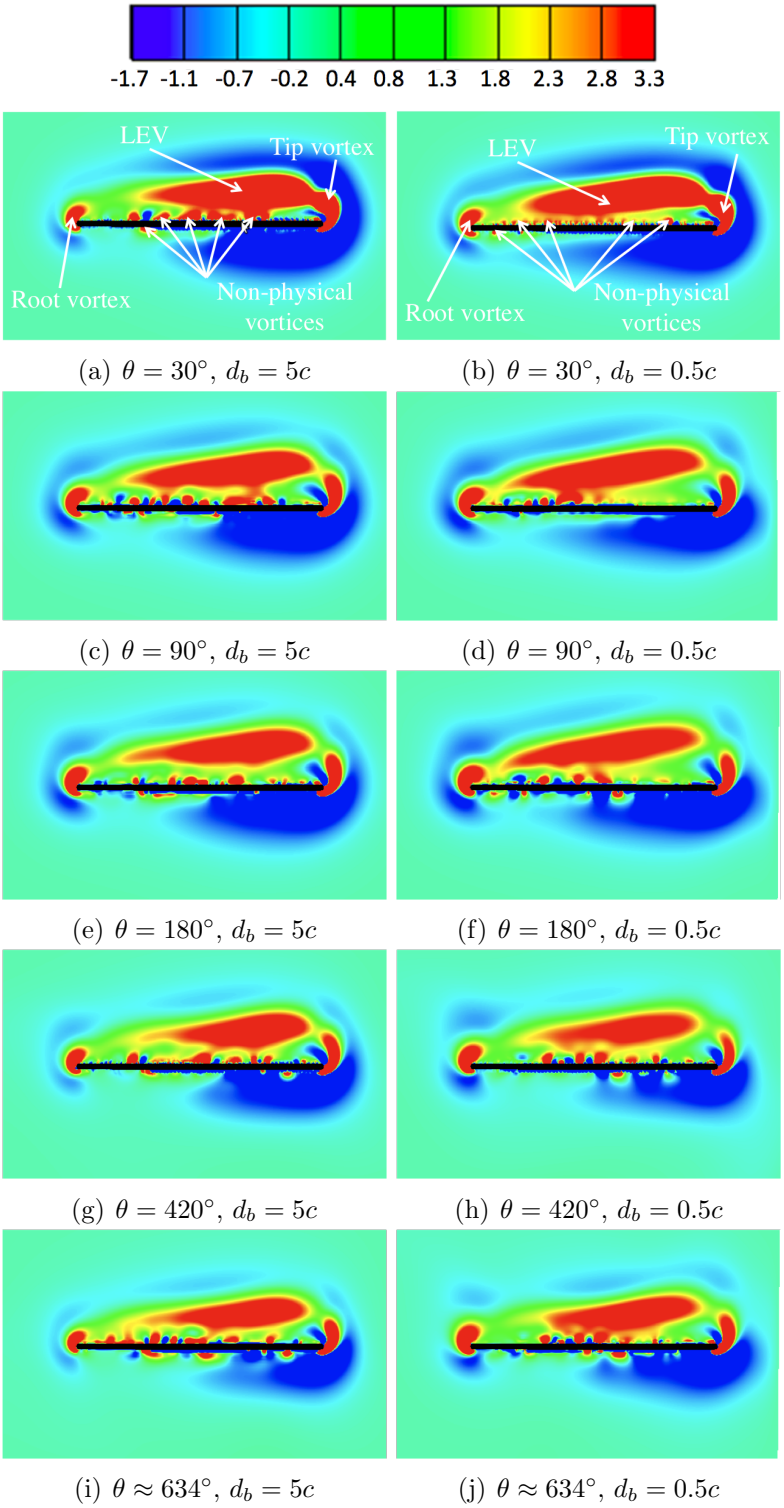

(a) $\theta = 30°$, $d_b = 5c$ (b) $\theta = 30°$, $d_b = 0.5c$

(c) $\theta = 90°$, $d_b = 5c$ (d) $\theta = 90°$, $d_b = 0.5c$

(e) $\theta = 180°$, $d_b = 5c$ (f) $\theta = 180°$, $d_b = 0.5c$

(g) $\theta = 420°$, $d_b = 5c$ (h) $\theta = 420°$, $d_b = 0.5c$

(i) $\theta \approx 634°$, $d_b = 5c$ (j) $\theta \approx 634°$, $d_b = 0.5c$

Figure 3.3: Spanwise views of Q-criterion, at quarter-chord for the $5.0c$ (left) and $0.5c$ (right) boundary conditions.

trailed vorticity. This is true for both the $0.5c$ and $5.0c$ boundary cases shown, as well as the $3.0c$ and infinite boundary cases, which are not shown. However, it is very hard to distinguish any significant differences among the boundary cases for a given rotation angle. The size, strength, and location of all important flow features, including the LEV, root vortex, and tip vortex, are very similar despite the variation in tip clearance among the cases.

However, when contours of vorticity, instead of Q-criterion, are plotted near the wing tip for infinite and half chord boundary cases, some differences can be seen in the size and shape of the tip vortex between the boundary cases, as shown in Figure 3.4. In this figure, the wing is again rotating into the page, with the midspan of the wing on the left of the figure and the wing tip on the right, such that only the outboard half of the wing is shown. In the first revolution, the size and shape of the tip vortex look very similar for the $0.5c$ and infinite boundary cases. However, in the second revolution, the tip vortex for the $0.5c$ case appears slightly elongated (taller and thinner) when compared to the infinite case.

A similar observation can be made when contours of the spanwise velocity are plotted, as shown in Figure 3.5. Here, blue contours show flow toward the root (left) and red/yellow contours indicate flow toward the wing tip (right). Even after 94 deg (Figure 3.5(a)-(b)) some differences in the spanwise velocity contours are evident between the $0.5c$ case and the infinite case. Both cases show a region of fluid flow from the wing root to the tip on the top surface of the wing, which coincides with the location of the LEV. However, the infinite case appears to have a slightly higher flow velocity over the midspan of the wing. Additionally, there is a region of fluid

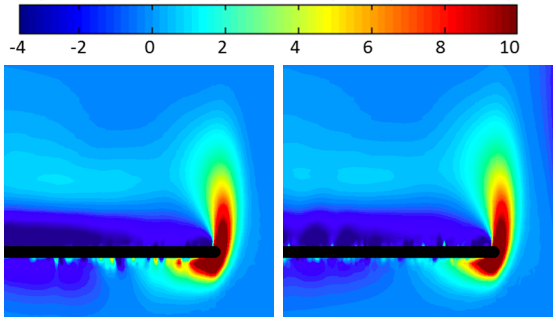

(a) $\theta \approx 94°$, $d_b = \infty$ (b) $\theta \approx 94°$, $d_b = 0.5c$

(c) $\theta \approx 634°$, $d_b = \infty$ (d) $\theta \approx 634°$, $d_b = 0.5c$

Figure 3.4: Quarter-chord slices of vorticity (s^{-1}) near the wing tip for the infinite boundary condition (left) and half-chord boundary condition (right).

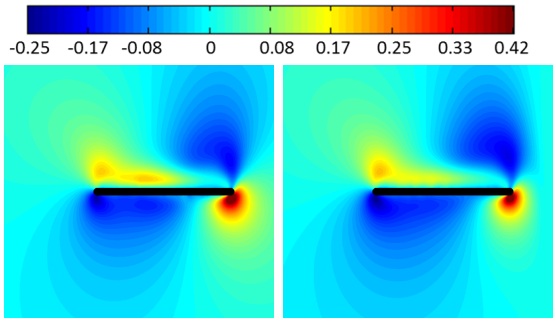

(a) $\theta \approx 94°$, $d_b = \infty$ (b) $\theta \approx 94°$, $d_b = 0.5c$

(c) $\theta \approx 634°$, $d_b = \infty$ (d) $\theta \approx 634°$, $d_b = 0.5c$

Figure 3.5: Quarter-chord slices of horizontal velocity, shown as a percentage of the tip velocity, for the infinite boundary condition (left) and $0.5c$ boundary condition (right).

flow toward the root located near the wing tip, which coincides with the location of the tip vortex. Some differences are also noticeable in the second revolution, in Figure 3.5(c)-(d). The $0.5c$ case, on the right, shows an increased region of flow toward the tip on the top surface of the wing near the wing root and over the wing midspan. Additionally, the $0.5c$ case has more flow toward the root on the bottom surface of the wing.

3.4 Aerodynamic Forces

The aerodynamic forces on the wing were found by using the pressure and velocity at every grid node on the surface of the wing to calculate normal and tangential force components, where the normal force is due to a pressure differential on opposing wing surfaces, and the tangential force is a result of the shearing of the fluid over the wing surface. These forces were decomposed into vertical lift and horizontal drag forces. The unsteady force coefficients were then determined by normalizing the lift and drag. This was accomplished by assuming the force coefficients, $C_f = \{C_l, C_d\}$, are constant along the wing span, in which case the force, F, can be determined by integrating the force coefficients from the wing root to the wing tip, $F = \int_{r_\mathrm{r}}^{r_\mathrm{t}} \frac{1}{2}\,\rho\,c\,C_f\,U(r)^2\,\mathrm{d}r$. Integrating and solving for the force coefficients yields $C_F = 6\,F/\left[\rho\,\Omega_{\max}^2 c\,(r_\mathrm{t}^3 - r_\mathrm{r}^3)\right]$. This method for force normalization is the root-relative method described in Chapter 2.

Figure 3.6 shows the lift and drag coefficients produced throughout two revolutions for all four boundary conditions. The data shown here was filtered using a fourth order lowpass Butterworth filter with a cutoff frequency of 10 Hz to eliminate effects of grid noise. Because the fluid mesh does not conform to the surface of the wing, points that were inside the wing surface on one time step and are outside the wing surface on the next time step can artificially affect the pressure at those points, leading to fluctuations in the forces as the wing moves. Furthermore, non-physical peaks in the forces were observed every 90 deg of rotation, when the spanwise axis of the wing is aligned with the x- or y-axis. To mitigate this, a 0.2 second moving aver-

age was applied to the data, smoothing the lift and drag curves over approximately 5.5 deg of rotation at the maximum angular velocity.

Both the lift and drag coefficients show a large initial spike, a result of the added mass effect caused by initial acceleration of fluid in front of the wing. This spike occurs at 3.0 deg for both the lift and drag coefficients, corresponding to the time the wing acceleration ends and the wing begins rotating at a constant velocity. After decreasing from the local maximum at the end of wing acceleration, the forces reach a local minimum around 20 deg. After recovering from this minimum, the forces reach a plateau and maintain a relatively constant value for the remainder of the first revolution. When starting the second revolution, the lift and drag coefficients decrease as a result of wake encounter, and level off after 540 deg. For the $0.5c$ boundary case, the lift coefficient levels off much sooner than the other three cases, resulting in a smaller overall decrease in lift coefficient.

In order to further study the decrease in force coefficients in the second revolution, average forces during the middle of the first revolution, between 90 and 270 deg, and during the second half of the second revolution, between 540 and 720 deg were calculated. This data is presented in Table 3.1 along with the percent change in lift and drag coefficients between the first and second revolutions for each case.

As seen in Figure 3.6, the lift and drag coefficients for the $0.5c$, $3.0c$ and $5.0c$ cases depart from the force coefficients in the infinite case after the recovery from the non-circulatory peak. This means that the averaged lift coefficient for the the $0.5c$, $3.0c$ and $5.0c$ cases are 0.2 higher (8% higher) than the averaged lift coefficient for the infinite case. Similarly, with the drag coefficient, in the first revolution the

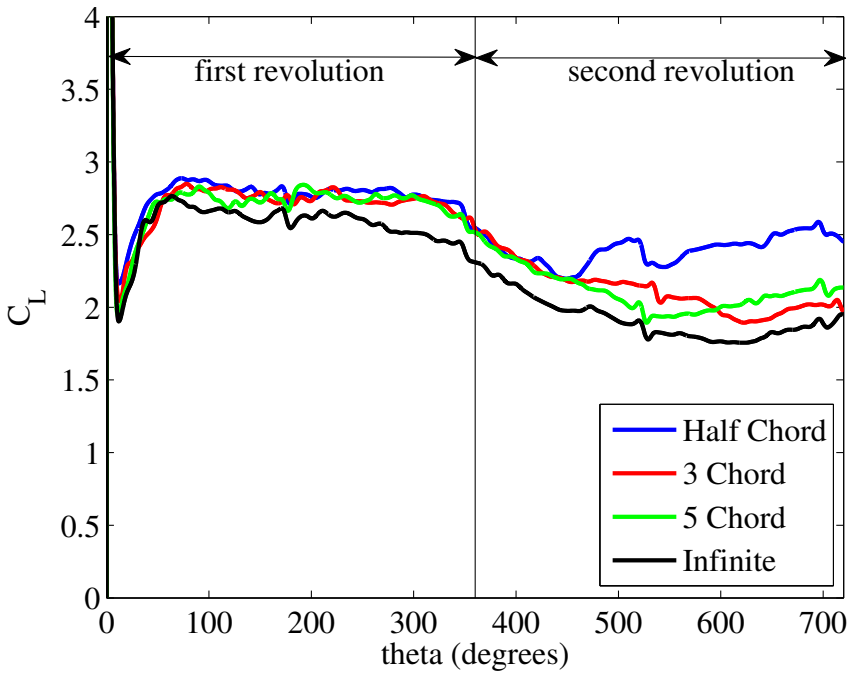

(a) Lift coefficient

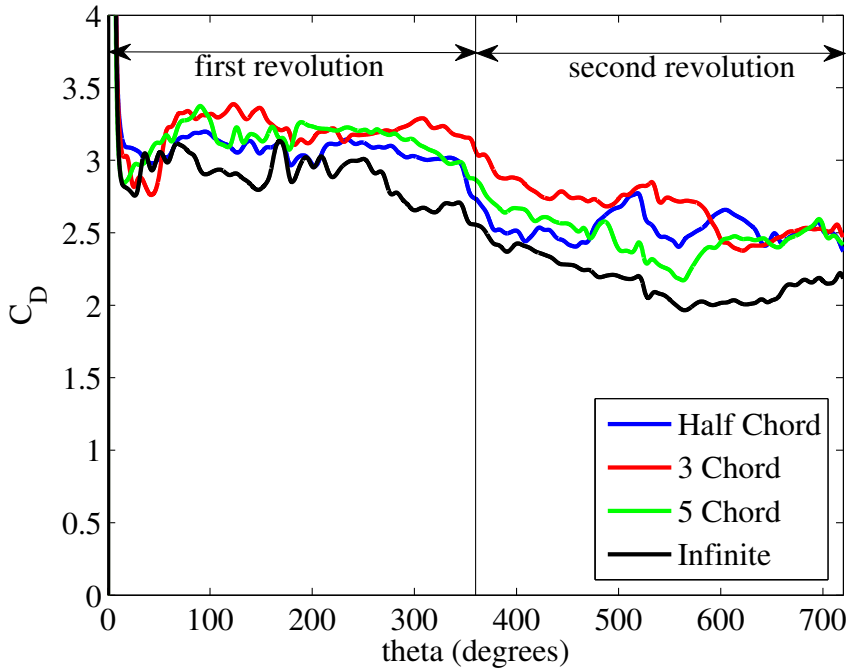

(b) Drag coefficient

Figure 3.6: Force coefficients as a function of wing stroke angle for $d_b = 0.5c$, $3.0c$, $5.0c$, and ∞.

Table 3.1: Average lift and drag coefficients in the first and second revolution of the wing stroke.

Boundary Condition	Lift Coefficient			Drag Coefficient		
	First Revolution	Second Revolution	Percent Change	First Revolution	Second Revolution	Percent Change
$0.5c$	2.8	2.4	-13%	3.1	2.5	-19%
$3.0c$	2.8	2.0	-29%	3.2	2.5	-22%
$5.0c$	2.8	2.0	-29%	3.2	2.4	-25%
Infinite	2.6	1.8	-32%	2.9	2.1	-28%

$5.0c$ and $3.0c$ cases have a drag coefficient that is 0.3 higher (18% higher) than the infinite case, and the $0.5c$ drag coefficient is 0.2 higher (14% higher). When the wing enters the second revolution, the lift and drag coefficients drop for all cases. The lift coefficient for the infinite case drops from an average of 2.6 in the first revolution to 1.8 in the second revolution, which is a decrease of 32%. The drag coefficient for the infinite case drops 28% from the first revolution to the second revolution. The drop in lift and drag coefficients from the first to the second revolution for the $5.0c$ case are 29% and 25%, respectively, which are very close to the decline percentages for the infinite case. However, the force coefficients for the $0.5c$ case drop significantly less, only 13% for lift and 19% for drag.

The $0.5c$ case approximates the infinite case as well as the $5.0c$ case does in the first revolution. But, by the second revolution, the force coefficients between the $0.5c$ case and the infinite case are very different, while the difference between the force coefficients for the $5.0c$ and infinite cases are the same in the second revolution as they are in the first.

This suggests that sizing the wing such that the tank walls are $5.0c$ from the wing tip will yield similar force trends to the case where no walls are present, but the lift and drag coefficients will be slightly elevated. The difference in force coefficients between the $0.5c$ case and the infinite case in the first revolution are quite small, 0.2 for both lift and drag, but much larger in the second revolution, 0.6 for lift, and 0.4 for drag, indicating that for rotation angles less than 360 deg, a tip clearance of $0.5c$ is large enough to approximate the case with no walls, but for two revolutions, the influence of the walls on the force history is too large for the wall effects to be considered negligible.

3.5 Vortex Circulation

To calculate the effects of the tank walls on the size and strength of the LEV throughout wing rotation, the γ function developed by Graftieaux et al. was used [42]. This function defines the quantity γ as a weighted average of the sine of the angle between the vectors extending from the point where γ is defined to a neighboring point and the in-plane velocity vector at that point. Thus, if the flow around a given point creates circular streamlines, then it has a value of $\gamma = 1$ or -1. γ is explicitly calculated through the formula

$$\gamma(P) = \frac{1}{S} \int_{M \in S} \frac{(\overrightarrow{PM} \times \overrightarrow{U_M} - \overrightarrow{U_P}) \cdot \hat{z}}{\left\|\overrightarrow{PM}\right\| \cdot \left\|\overrightarrow{U_M} - \overrightarrow{U_P}\right\|} \mathrm{d}S = \frac{1}{S} \int_S \sin(\theta_M) \mathrm{d}S, \tag{3.2}$$

which is calculated at every point P in the flow field. Any point where $|\gamma(P)|$ is greater than a certain threshold value, usually 0.6, is considered part of a vortex. For every boundary case, chordwise slices at the midspan for every rotation angle where

a velocity field was produced (approximately every 10 deg) were used to calculate γ fields. The LEV was defined as the largest continuous region of discrete points where $|\gamma|$ exceeded a certain value, and the center of the LEV was defined as the point inside the LEV that had the highest γ value. The total circulation inside the LEV was then calculated by summing the vorticity of each element inside the $|\gamma| \geq \gamma_{cutoff}$ contour multiplied by the size of the local grid element area:

$$\Gamma_{LEV} = \sum_{i=1}^{n} (\vec{\nabla} \times \vec{v}_i) dx_i dy_i,$$

where Γ_{LEV} is the in-plane circulation contained in the LEV slice taken at half span, n is the number of grid elements inside the LEV, $\vec{\nabla}$ is the two dimensional del operator, $\vec{v}$ is the planar velocity vector, and dx and dy are the width and height of each fluid element.

Figure 3.7(a) shows the circulation of the LEV as a function of rotation angle assuming a variety of γ values as the cutoff for what is considered a vortex. Thus, a point where $\gamma = 0.61$ would be considered inside the LEV for a cutoff value of $\gamma \geq 0.6$ but outside the LEV for a cutoff value of $\gamma \geq 0.7$. As long as the γ cutoff value is less than 0.9, all cutoff values result in similar trends for the growth of circulation within the LEV. The circulation of the LEV rises quickly from zero when the wing is at rest until 60 deg, after which the growth of circulation slows significantly. The strength of the LEV then remains relatively constant throughout the remainder of the first revolution, and drops steadily for the first half of the second revolution. After that, the circulation of the LEV again remains relatively constant for the remainder of the second revolution. There is a fair amount of noise

present in this data that can be attributed to one main cause. The boundary of the leading edge vortex is calculated independently for each time step, which may have led to varying LEV boundaries from one time step to the next. Thus, certain clumps of circulation, especially the non-physical circulation on the surface of the wing, are defined as in the leading edge vortex at one time and out of the leading edge vortex a time δt later.

In Figure 3.7(b), the γ threshold value is plotted against the circulation of the LEV at one rotation angle, 186 deg (see vertical dotted line in Figure 3.7(a)) for γ cutoff values ranging from 0.35 to 0.95 in increments of 0.5. This figure illustrates that there is a linear relationship between γ threshold value and circulation between $\gamma = 0.35$ and $\gamma = 0.7$, as illustrated by the best fit line for these data points shown in red. At cutoff values greater than 0.7, the circulation of the LEV drops sharply until no grid elements have a high enough γ value to be considered part of the LEV (around $\gamma = 0.9$). Based on this information, a γ cutoff value of 0.7 was chosen to define the LEV.

The circulation was then plotted versus rotation angle for each boundary case, as shown in Figure 3.8. The vertical dotted lines labeled A-E in this figure correspond to the rotation angles shown in the Q-criterion plots of Figure 3.2. For all of the cases, the circulation follows the trends described previously for the $5.0c$ case at γ values greater than 0.9. Additionally, the evolution of circulation appears to closely follow many of the trends associated with the lift coefficient history, including a steep rise early in the wingstroke and a drop at the beginning of the second revolution. Similar to with the lift coefficient, the infinite boundary case has an

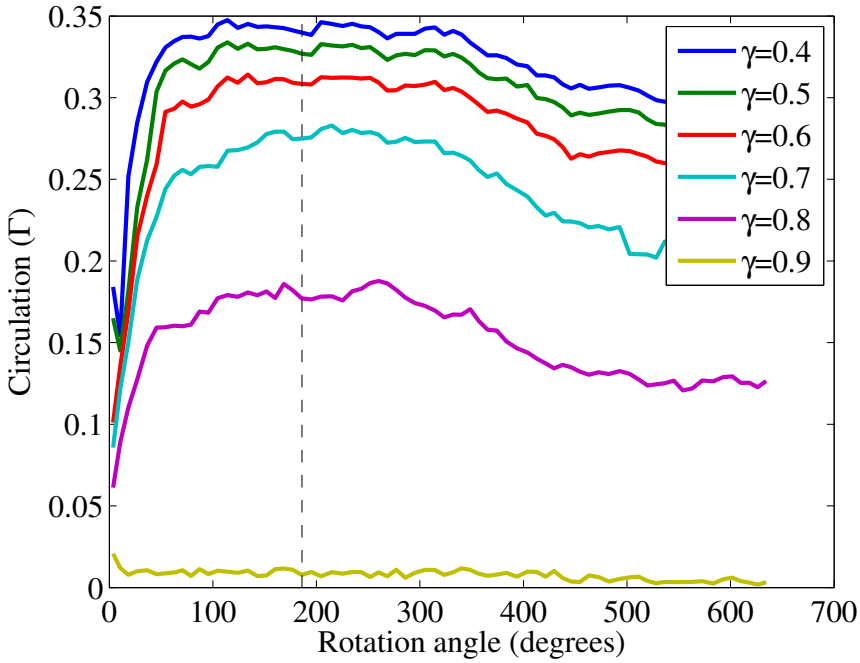

(a) LEV circulation as a function of stroke angle

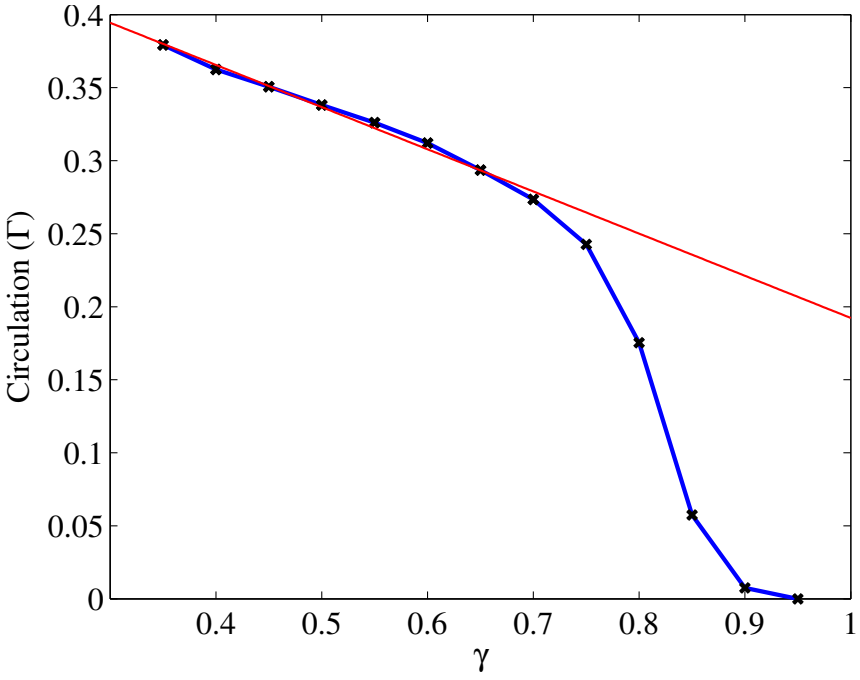

(b) LEV circulation at $\theta = 186°$ versus γ threshold value

Figure 3.7: Circulation of the LEV at half-span and $d_b = 5.0c$ as defined by a range of γ values.

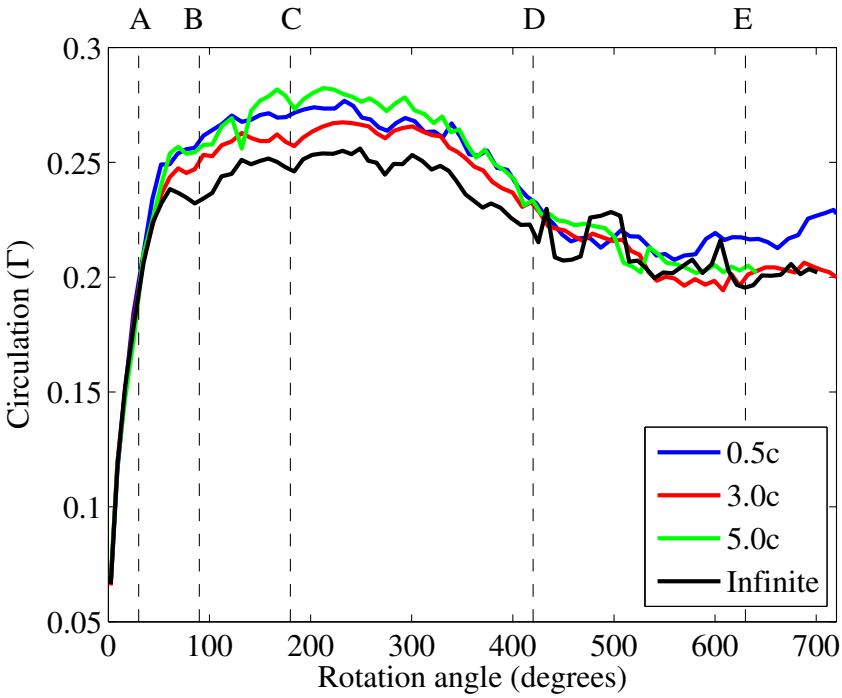

Figure 3.8: Circulation of the LEV as a function of stroke angle for $d_b = 0.5c$, $3.0c$, $5.0c$, and ∞.

average circulation in the first revolution that is slightly lower than the other three. Also, at the end of the second revolution, the circulation of the LEV for the $0.5c$ case is higher than for the other three cases, as is true with the lift coefficient.

3.6 Wake Effects

Regardless of how far tank walls are placed from the wing tip, a noticeable decline in both forces (Figure 3.6) and LEV circulation (Figure 3.8) was observed at the beginning of the second revolution. A reasonable hypothesis for explaining this phenomenon is that the wake the wing creates on the first revolution interacts with the wing when it begins its second revolution. If the wake results in downwash on the wing, the reduced effective angle of attack in the second revolution could cause a decline in forces and vorticity strength. In order to examine the validity of this hypothesis, a more in-depth analysis of wake effects was performed.

Figure 3.9 shows chordwise slices of vertical velocity at the midspan for all four boundary conditions at 94 deg and 634 deg. Red contours indicate a large upward velocity, while blue contours indicate a large downward velocity. The wings shown are moving from left to right, so the right side of the figure shows the velocity field of the fluid that the wing is about to encounter. In front of the wing, after 94 deg of rotation (a-d), there is quiescent fluid (yellow), except for near the leading edge, where the fluid has a slight upward velocity as it prepares to flow up and around the leading edge of the wing. This is true for all boundary conditions. After 634 deg of rotation (e-h), we can see some variations in the vertical velocity fields as a result

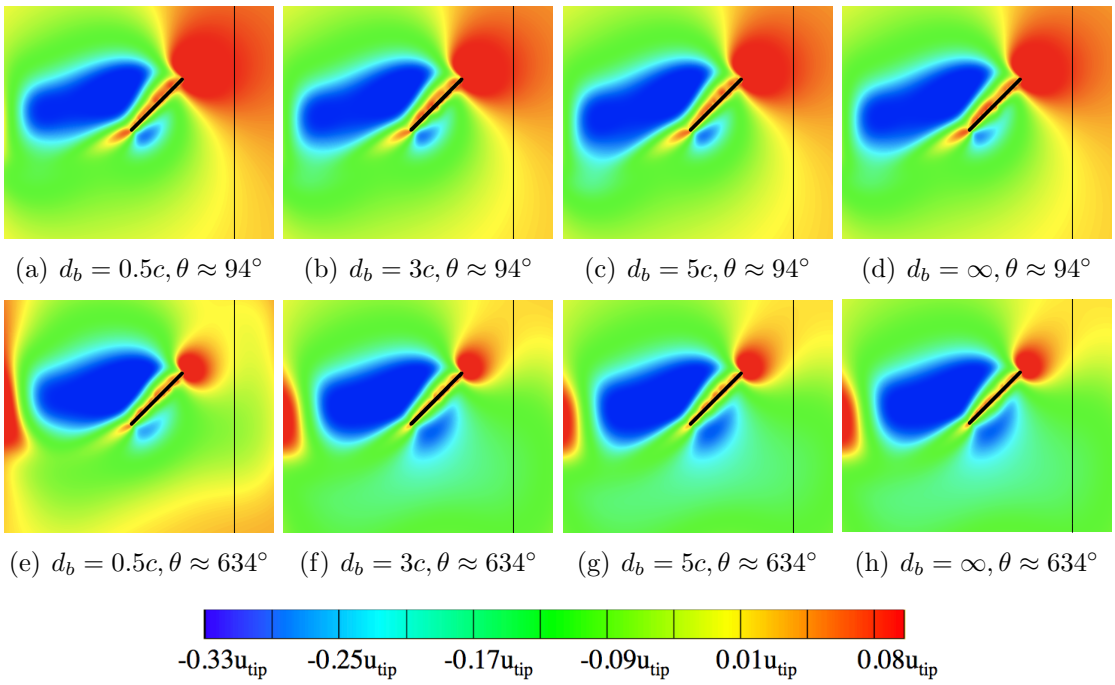

(a) $d_b = 0.5c, \theta \approx 94°$ (b) $d_b = 3c, \theta \approx 94°$ (c) $d_b = 5c, \theta \approx 94°$ (d) $d_b = \infty, \theta \approx 94°$

(e) $d_b = 0.5c, \theta \approx 634°$ (f) $d_b = 3c, \theta \approx 634°$ (g) $d_b = 5c, \theta \approx 634°$ (h) $d_b = \infty, \theta \approx 634°$

Figure 3.9: Contours of vertical velocity at mid-span for $d_b = 0.5c$, $3.0c$, $5.0c$ and ∞ in the first ($\theta \approx 94°$, top) and second ($\theta \approx 634°$, bottom) revolutions.

of the boundary conditions. For the infinite case (h), a large region of downward velocity in front of and below the wing is present. This region looks very similar for the $5.0c$ and $3.0c$ boundary cases. However, this region of downwash is much smaller for the $0.5c$ case. This suggests that walls close to the wingtip suppress some of the downwash created by the wake.

The relative strength of the downwash can also be visulalized by plotting the magnitude of the vertical velocity along a vertical line one chord ahead of the midspan of the wing, shown by the vertical black lines in Figure 3.9. This is shown in Figure 3.10. In this figure, the y-axis shows the vertical position (in chords above/below the wing mid-chord) along the black lines shown in Figure 3.9. The x-axis shows the magnitude of the vertical velocity along that line, where upwash is to the right and downwash is to the left. After 94 deg of rotation, the velocity one chord-length in front of the midspan of the wing is identical for the infinite, five chord, and three chord boundary condition cases. Although the half chord case deviates slightly, it still exhibits the same trends as the other three cases: The vertical velocity is zero far above and below the wing, and at the wing midchord, there is a slight upward velocity, equal to 3.1% of the half span velocity for the infinite, five, and three chord cases and 4.1% of the half span velocity for the half chord case. In the second revolution, a significantly different vertical velocity profile in front of the wing is observed. While all four cases have zero vertical velocity far above and below the wing, the infinite, five and three chord cases have a strong downwash slightly below the wing midchord, and the half chord case has a very small upwash above the wing midchord and a small downwash slightly below midchord.

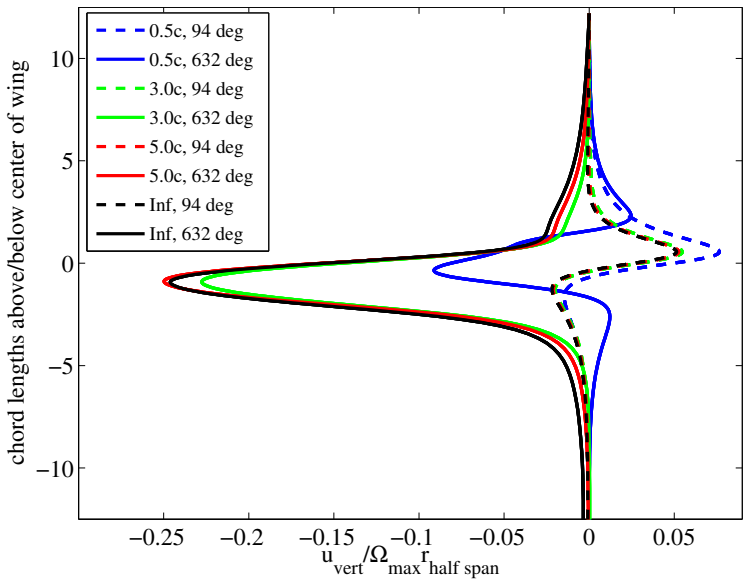

Figure 3.10: Vertical velocity one chord-length in front of wing, $\theta \approx 94°, 634°$.

The maximum upwash velocities in the first revolution and maximum downwash velocities as in the second revolution are summarized in Table 3.2. Velocities in this table are given as a percentage of the wing midspan velocity. It is evident that in the first revolution, after 94 deg, even the half chord case deviates only slightly from the case with no wall boundaries, whereas by the second revolution, only the $3.0c$ and $5.0c$ cases closely resemble the infinite case.

Another way to visualize the wake created by the wing as it rotates is to examine horizontal slices of the vertical velocity. The location of this slice plane is shown in Figure 3.11. In this figure, the wing is rotating counterclockwise when viewed from above about the z-axis, and the leading edge is highlighted in red. The grey surface, parallel to the xy-plane, shows the location of the horizontal slice, just

Boundary Condition	Maximum upwash in first revolution	Maximum downwash in second revolution
Half-Chord	4.6%	9%
3-Chord	3.1%	23%
5-Chord	3.1%	25%
Infinite	3.1%	25%

Table 3.2: Maximum vertical velocity one chord-length in front of wing midspan.

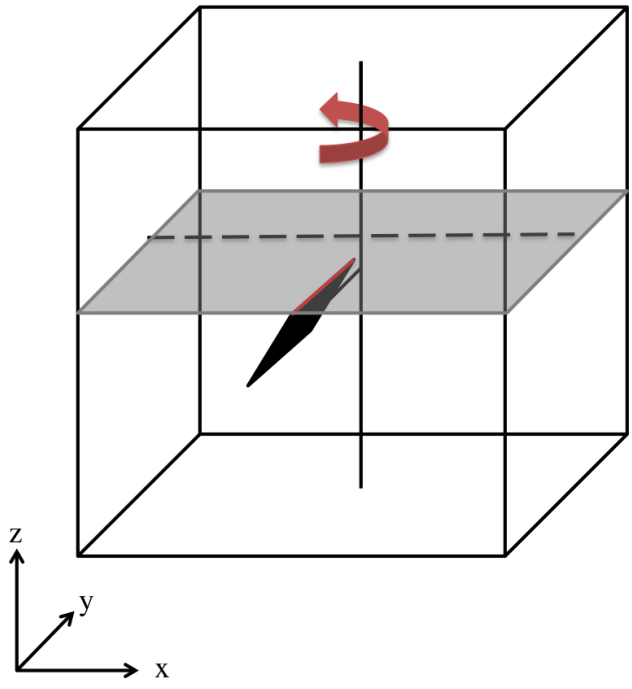

Figure 3.11: Location of horizontal slice plane and line through plane.

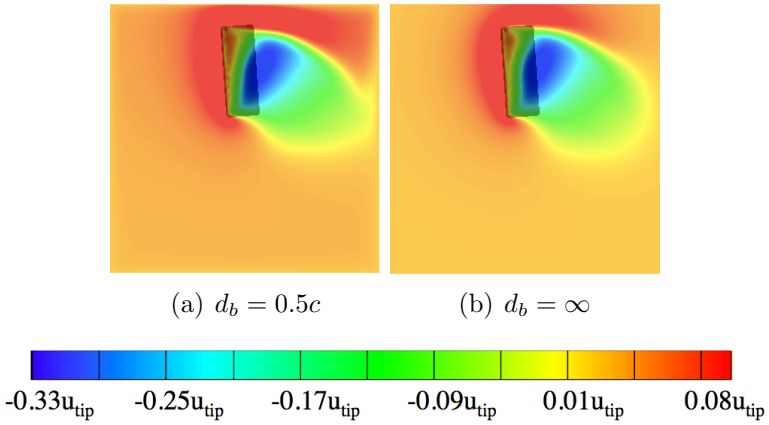

Figure 3.12: Contours of vertical velocity, $\theta \approx 94°$.

above the leading edge of the wing.

Figure 3.12 shows horizontal slices taken in this location after 94 deg of rotation for the half chord and infinite cases. The contours in this figure are of the velocity component normal to the slice, in the lift direction. A full cross-section of the $0.5c$ "tank" is shown. For the infinite case, a portion of the mesh equal in size to the cross section of the $0.5c$ mesh is shown. In these figures, the wing is rotating counterclockwise and red contours correspond to velocity up (out of the page), while blue corresponds to velocity down (into the page). No discernible differences can be observed between the two vertical velocity fields. The two cases not shown (the five and three chord cases) also look very similar.

Figure 3.13 shows the same horizontal slices of vertical velocity for all four cases after 634 deg of rotation. A full cross section of the half chord "tank" is shown. For the $3.0c$, $5.0c$, and infinite cases, a region equal in size to a cross-section of the $3c$ tank (larger than the $0.5c$ region) is shown, so that the whole wake structure can

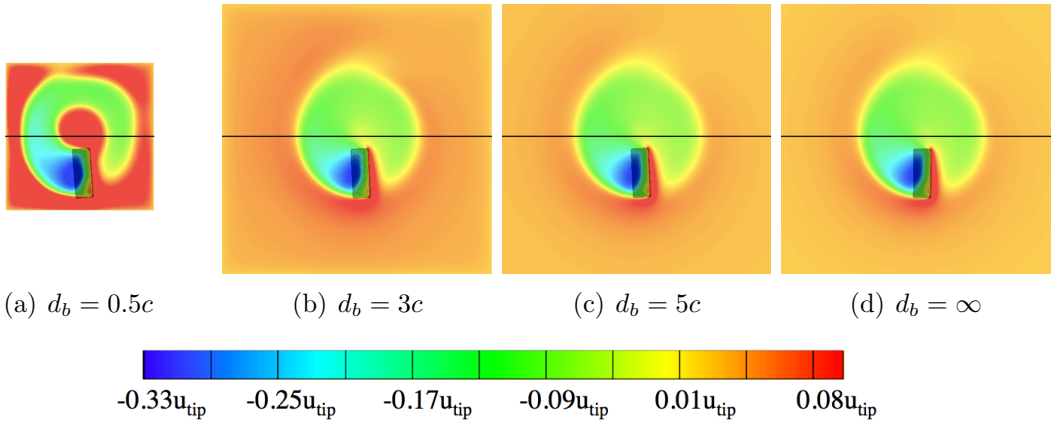

Figure 3.13: Contours of vertical velocity above the wing at $\theta \approx 634°$ for $d_b = 0.5c$, $3.0c$, $5.0c$ and ∞.

be visualized. For all four cases, the wake of the wing, shown in green, is the area swept out by the wing as it rotates. For the infinite and five chord cases, a region of fluid with zero vertical velocity (orange) surrounds the wake of the wing. Inside the wake, a small region of strong downwash exists just above the wing, while a weaker downward flow is seen in the entire region swept out by the wing. Also noticeable for the infinite, $5.0c$, and $3.0c$ cases (b-d) is a thin region of flow just outside the path swept out by the wing tip with a upward velocity (red). This region is presumably part of the tip vortex that has shed from the wing. This region is more pronounced for the $3.0c$ case (b). The $0.5c$ case (a) has a constricted region of downwash inside the wake due to upwash near the wing root (in red), which is not present for the other cases. Outside the area swept out by the wing tip, a region of upwash (in red) is also present, and extends to the tank walls.

The vertical velocity through the middle of the tank and just above the wing tip is taken along the black lines shown after 634 deg of rotation, and plotted in

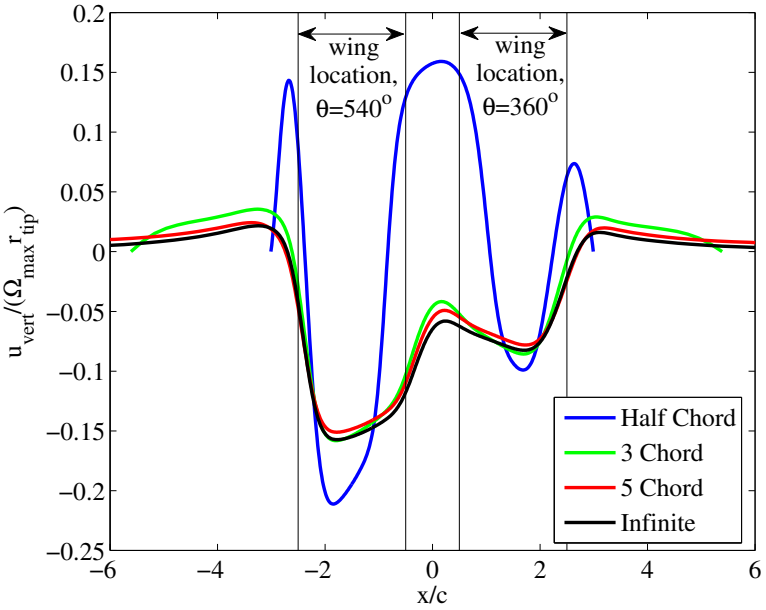

Figure 3.14: Vertical velocity above wing leading edge along the x-axis of the computational domain at $\theta \approx 634°$.

Figure 3.14. The location of this line is also illustrated by the dotted black line in Figure 3.11. In Figure 3.14, the vertical velocity, given as a percentage of the wing tip velocity, is plotted against the x-coordinate along the line, normalized by the wing chord length (x/c). In this figure, two regions are marked, indicating where the wing passed after 360 deg and after 540 deg. The area inside these regions coincides with the area inside the circle swept out by the wing root, and the two areas outside these regions correspond to the area outside of the circle swept out by the wing tip. The infinite, $5.0c$, and $3.0c$ cases, which are nearly identical, show an almost constant zero vertical velocity to the right of $x = 2.5c$ and to the left of $x = -2.5c$. The $3.0c$ case has a slightly higher velocity outside the wing wake than the $5.0c$ and infinite cases, however. A strong downwash is seen where the wing was after 540 deg, whereas the downwash in the region where the wing was after 360 deg is weaker due to dissipation and a longer time since the wing passed. The $0.5c$ case exhibits markedly different trends. A larger maximum downwash is observed in the wing wake, but inside the wing root path and outside the wing tip path, a strong upwash is present. Thus, after a long rotation time, at small tip clearances, the flow features of the rotating wing no longer resemble those of a wing rotating in an infinite volume of fluid.

3.7 Laser/Particle Flow Visualization

While this computational analysis was meant to address the effects of side walls on a wing rotating at low Reynolds numbers, most experimental setups have

further restrictions in the flow, including a tank bottom and either a solid wall at the top of the tank or a free surface. In order to examine the effects of the top and bottom surfaces on the flowfield produced by a rotating wing, particle imaging flow visualization was performed. As shown in Figure 2.4, the laser sheet was aligned to capture the entire tank cross section. All images shown are taken after a certain number of compete revolutions, when the midchord of the wing was aligned with the x-axis.

Figure 3.15 shows the $5c$ case after 1 (a), 2 (b), 6 (c), and 16 (d) revolutions. In the first image, the size and location of the wing are represented by a black rectangle, which is the same for all images. The major flow features are highlighted by white arrows. After one revolution, the flowfield consists of a vortex ring with a radius of approximately $2.5c$, which coincides with the location swept out by the wing tip. After 2 revolutions, this vortex ring has grown in size. This trend continues until the wing has completed 6 revolutions, and the vortex ring has grown so large that it touches the tank walls. After 6 revolutions, the flowfield remains very similar until 16 revolutions, when a counter rotating vortex ring develops below the primary vortex ring. The secondary ring extends from just below the bottom of the primary ring to the bottom of the tank. This flowfield remains as shown through 45 revolutions, when the wing rotation ended.

Because the computational study examined wing rotation up to two revolutions, it is convenient to compare the flowfield for the $5.0c$, $3.0c$, and $0.5c$ cases side by side, as shown in Figure 3.16. Different sized wings (c =1.2 in for the $5.0c$ case, 1.64 in for the $3.0c$ case, and 3.0 in for the $0.5c$ case) were used to achieve the

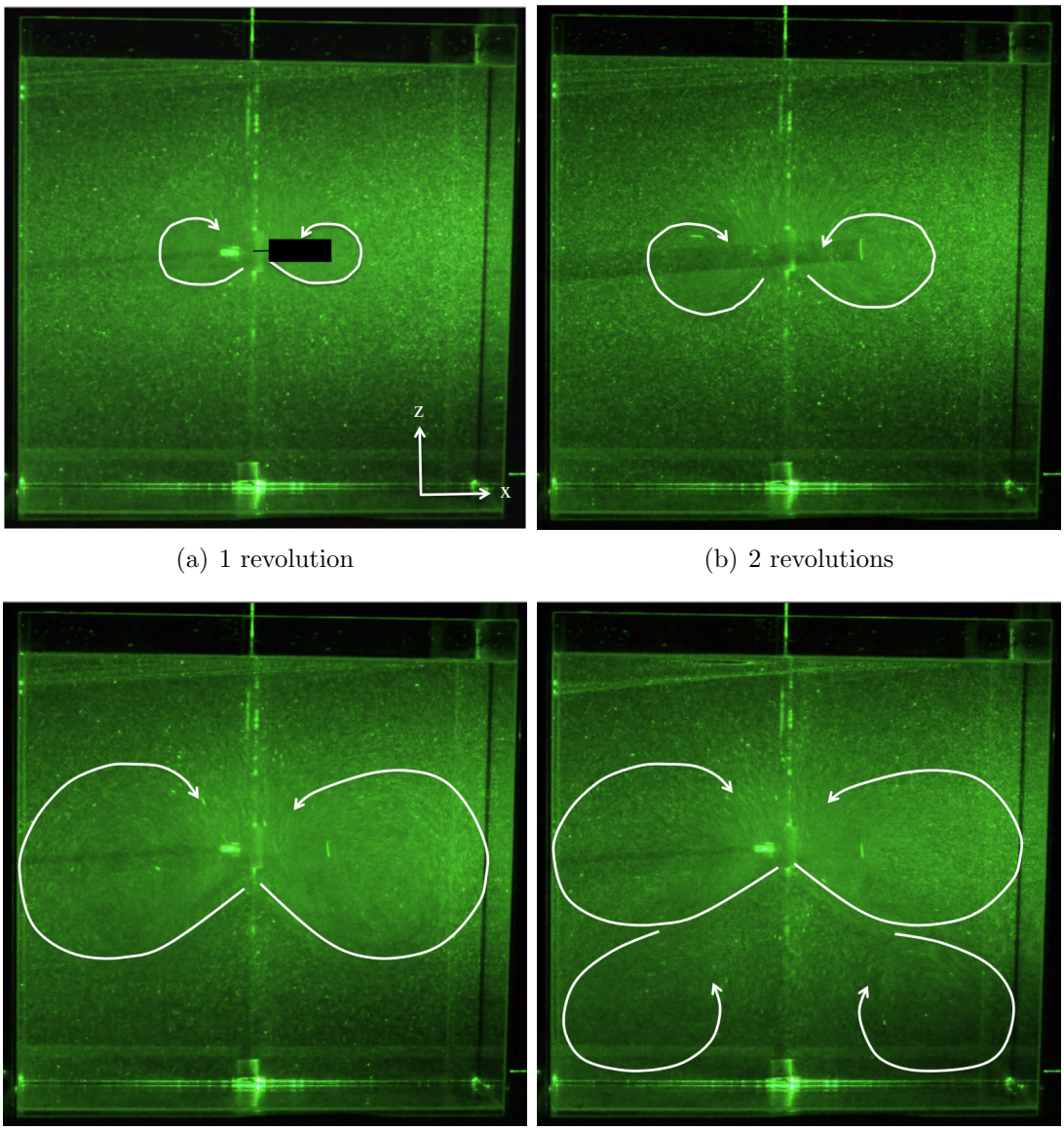

(a) 1 revolution

(b) 2 revolutions

(c) 6 revolutions

(d) 16 revolutions

Figure 3.15: Flow visualization of tank cross-section for rotating wing with $5c$ tip clearance up to 16 revolutions.

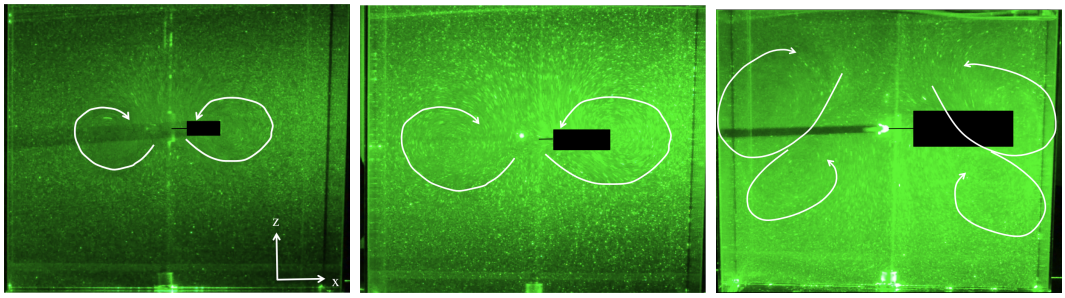

(a) $d_b = 0.5c$ (b) $d_b = 3c$ (c) $d_b = 5c$

Figure 3.16: Flow visualization of tank cross-section for rotating wing with varying tip clearance after two revolutions.

varying tip clearances, so the wing in all three cases has been represented by a black rectangle. The maximum velocity for each case was set to maintain a tip Reynolds number of 120. After two revolutions, the flowfield for the $5.0c$ case (a) consists of a single vortex ring that is smaller in diameter than the tank width. This is the same image as shown in Figure 3.15, except with wing shown. For the $3.0c$ case (b) a single vortex ring also exists. While this vortex ring is larger than for the $5.0c$ case, it is approximately the same size in terms of wing chord lengths in diameter. For the $0.5c$ case, a counter-rotating vortex ring is visible in addition to the primary vortex ring, which has already impacted the tank wall. However, the secondary vortex ring has not extended down to the bottom of the tank, as in the $5.0c$ case after 16 revolutions. It is therefore reasonable to assume that even for the $0.5c$ case, where the bottom of the tank is located $3.0c$ below the wing midchord, that the bottom does not have a strong influence on the flowfield of or forces generated by the rotating wing for up to two revolutions.

3.8 Summary

This chapter presented results from a computational study analyzing the effect of tip clearance on a wing rotating in a square tank, as well as laser/particle flow visualization examining the flowfield in a cross section of the tank for varying tip clearances. In the computational study, tip clearances of $d_b = 0.5c$, $3.0c$, $5.0c$, and ∞ were examined, while the flow visualization examined tip clearances of $d_b = 0.5c$, $3.0c$, and $5.0c$. Looking at chordwise and spanwise slices of Q-criterion, a measure of vorticity, very few differences were noticeable at a given rotation angle among any of the tip clearances studied.

An analysis of the lift and drag produced in the computational study showed that even walls placed $5.0c$ from the wing tip increased the lift and drag coefficients by approximately 8% over the infinite case, beginning after the recovery from the non-circulatory peak. However, the shape of the force coefficient curves and the flow features for the $5.0c$ case were very similar to the infinite case for up to two revolutions. The $0.5c$ case matched the infinite case well in the first revolution, but both the force coefficients and the flow structures diverged quickly from the infinite case beginning in the second revolution. The $3.0c$ case also showed divergence from the infinite case toward the end of the second revolution in the flow features. Therefore, for examining flows up to two revolutions, a minimum tip clearance of $5.0c$ is necessary for approximating the case where no wall boundaries are present.

The laser/particle flow visualization showed that the primary flow feature associated with a rotating wing is the production of a ring-like vortex near the path

swept out by the wing tip, presumably the trailing tip vortex. This vortex grows as the wing travels for greater numbers of revolutions, and eventually, the ring-like vortex impinges on the tank walls. After that, a secondary, counterrotating ring-like vortex is formed below the primary vortex, and eventually impinges on the bottom of the tank. Visualization of the $0.5c$, $3.0c$, and $5.0c$ cases shows that the bottom surface of the tank has a minimal influence on the flowfield after two revolutions, the maximum rotation studied in both the computational analysis of this chapter and the force measurement analysis presented in Chapter 4.

Chapter 4

Aerodynamic Force Analysis

4.1 Overview

A parameter study was performed to analyze the influence of maximum rotation angle, acceleration profile, and root cutout on the aerodynamic forces generated by a fixed-pitch rotating wing. Force data was acquired using a six degree-of-freedom force/torque sensor. Lift and drag coefficient histories were computed from the raw data using both the axis-relative and root-relative methods described in Chapter 2, and compared to forces produced by both translating and rotating wings at the Air Force Research Lab (AFRL) Horizontal Free-Surface Water Tunnel facility.

4.2 Variation in Maximum Rotation Angle

Figure 4.1 shows the force coefficients for a wing with $0.5c$ root cutout accelerating over one chord-length at the axis-relative reference plane. The maximum angular velocity for each case was chosen such that the axis-relative Reynolds number was 10,000. Maximum rotation angles of 90, 180, 270, 360, 540, and 720 degrees were tested. In this figure, the left-most vertical dotted line indicates the point at which the wing would have reached a constant velocity if the velocity profile was unsmoothed. This is the same for all cases. The remainder of the dotted vertical black

lines indicate the points at which the wing would begin to decelerate if the velocity profile was unsmoothed, corresponding to 7.6 deg before the maximum rotation angle, or $0.25c$ traveled at the axis-relative reference plane. Although it appears that the force coefficients begin to drop steeply just before the start of wing deceleration, indicated by the vertical black lines, the smoothing present in the velocity profile means that the wing has actually started to decelerate at a position slightly before the vertical dotted black lines in the figure.

The lift and drag coefficients for all cases look very similar prior to wing deceleration. The force coefficients for all cases rise from zero to a local maximum at $s/c = 1.0$, where the wing reaches a constant velocity. This peak is the result of non-circulatory, or added mass, effects. While the wing is accelerating, the fluid in front of the wing must also be accelerated, resulting in a force peak when the wing stops accelerating. After a slight decline in force coefficients following the non-circulatory peak, the coefficients begin to rise toward a second, larger local maximum occurring at $s/c = 3.5c$ (107 deg of rotation). After this second local maximum, the force coefficients begin to decline and level out at $s/c = 4.9c$ (150 deg of rotation). After this point, the lift and drag remain relatively constant throughout the remainder of the first revolution. At the beginning of the second revolution, the force coefficients begin to drop. This decline is likely the result of the wing entering the wake created in the first revolution, as discussed in Section 3.6. After 540 degrees of rotation, the lift and drag forces level out to a relatively constant value for the second half of the second revolution.

Figure 4.1 demonstrates that the force coefficients on the rotating wing are

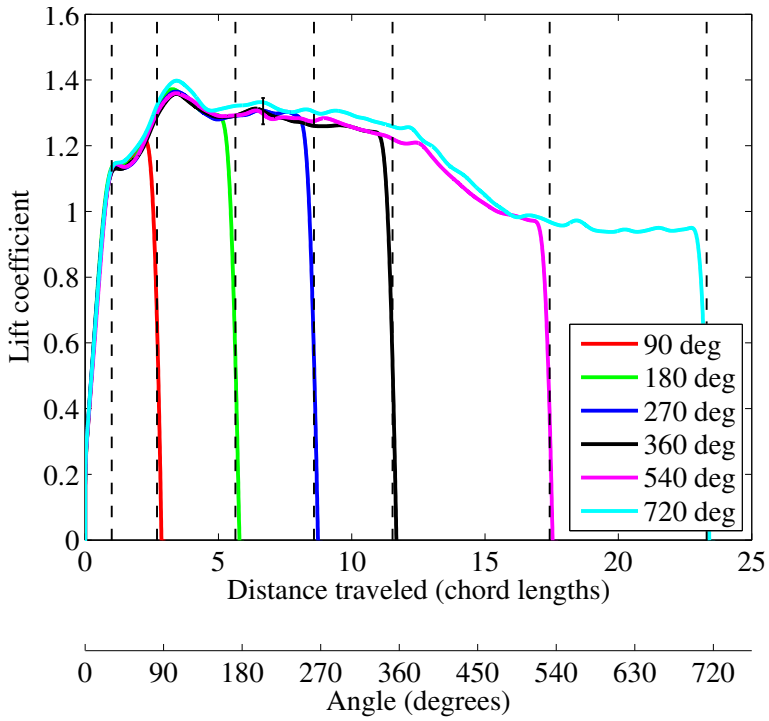

(a) Lift coefficient.

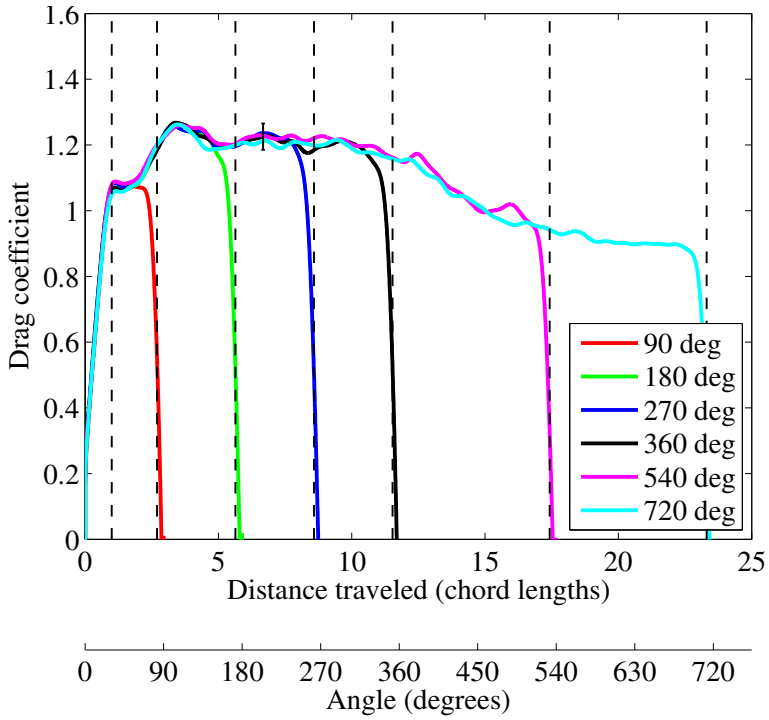

(b) Drag coefficient.

Figure 4.1: Force coefficients for maximum rotation angles of 90° (red), 180° (green), 270° (blue), 360° (black), 540° (magenta), and 720° (cyan).

independent of maximum rotation angle. This result is expected because the velocity profiles for the range of maximum rotation angles tested are identical prior to the start of wing deceleration. Also of note is that after 90 deg of rotation, which is the mechanical limit of many rotating wing rigs, the force coefficients are still rising toward the second local maximum. This suggests that the flow field is not fully developed at the maximum range of motion of past experiments. The force coefficient histories and the flow features associated with them are quite interesting and worth studying using a rig capable of much higher rotation angles, such as the one used for these experiments.

It is evident from Figure 4.1 that the lift and drag coefficient histories for a given maximum rotation angle are extremely similar. This occurs because the force normal to the wing is approximately one order of magnitude greater than the shear force along the surface of the wing. The lift and drag are related to the wing shear and normal forces through the equations $L = F_N \cos(\alpha) + F_S \sin(\alpha)$ and $D = F_N \sin(\alpha) + F_S \cos(\alpha)$, where L is lift, D is drag, F_N is the force normal to the surface of the wing, F_S is the force parallel to the wing surface. Thus, when α, the wing angle of attack, is 45 deg, as for these experiments, the resulting lift and drag forces are almost identical. The same trend of nearly identical lift and drag coefficients for a wing at a 45 deg angle of attack was seen by Dickinson and Gotz, when performing an angle of attack parameter sweep on a translating, aspect ratio 3 wing at Re=192 [20] and others [33].

4.3 Variation in Acceleration Profile

For the baseline case of a wing with a root cutout of $0.5c$ rotated to a maximum of 540 deg, a variety of acceleration distances ranging from $0.25c$ to $6.00c$ were studied. The force coefficients generated by all of these cases are shown in Figure 4.2. The acceleration distance, s_a/c, is defined as the length of the arc traversed by the point on the leading edge of the wing located at the reference plane when the wing reaches a constant velocity, normalized by the wing chord length. The right-most vertical dotted black line in Figure 4.2 indicates the wing deceleration for all cases. The remainder of the vertical dotted black lines correspond to the end of wing acceleration for each of the acceleration profiles tested. Regardless of the acceleration distance, throughout wing acceleration, the force coefficients rise at a near constant rate to a local maximum at the end of wing acceleration. The magnitude of this non-circulatory peak is greater for shorter acceleration distances. Because the maximum velocity for all cases is the same, a shorter acceleration distance corresponds to a greater acceleration, and a larger non-circulatory peak. For cases where $s_a/c \geq 2.00c$, the non-circulatory effects are small enough that this local maximum in force coefficients is indistinguishable after data processing and smoothing.

After the lift and drag coefficients recover from the first local maximum at the end of wing acceleration, the force coefficients are nearly identical regardless of the acceleration profile. The only significant difference is that, while the location of the second local maximum in the force coefficients is the same for acceleration distances

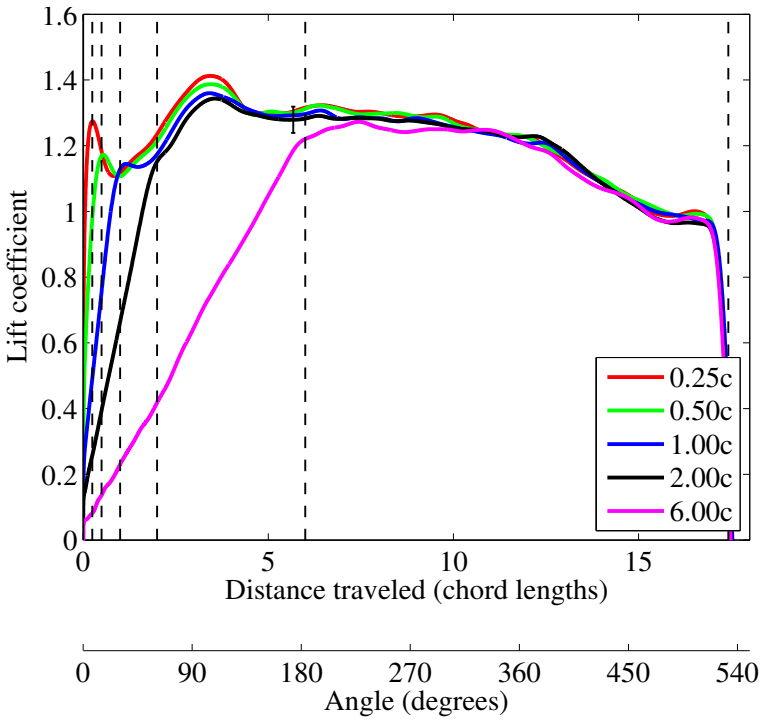

(a) Lift coefficient.

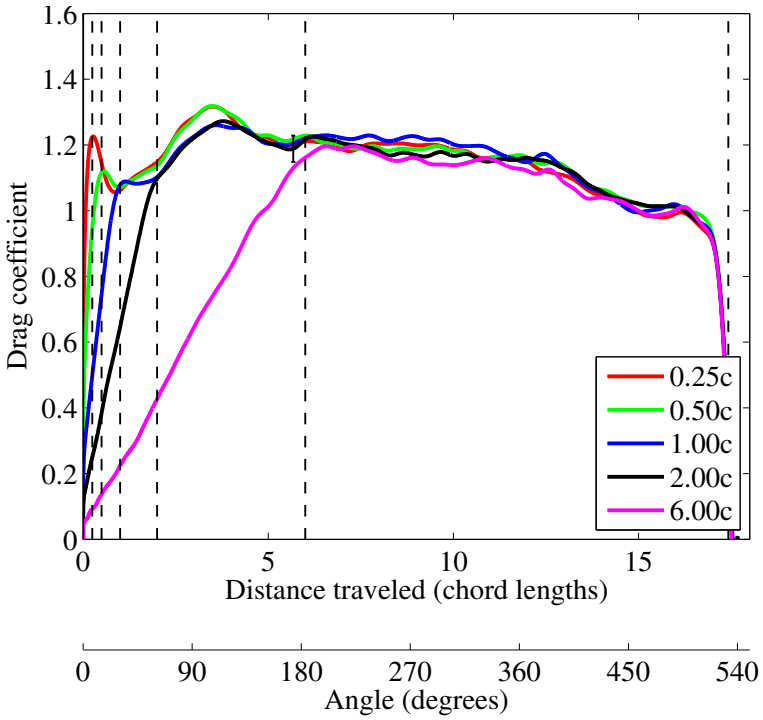

(b) Drag coefficient.

Figure 4.2: Force coefficients for acceleration distances of $0.25c$ (red), $0.50c$ (green), $1.00c$ (blue), $2.00c$ (black), and $6.00c$ (magenta).

between $0.25c$ and $2.00c$, the magnitude of this peak is slightly higher for shorter acceleration distances. For the $6.00c$ case, the wing is still accelerating after $3.5c$ traveled, where the second local maximum occurs for the other cases. No deviation from the linear increase in lift and drag coefficients is seen for this case at $3.5c$. This suggests that the flow features associated with the second local maximum in force coefficients are suppressed or not present if the wing is still accelerating, and only result in a local maximum in forces if the wing has already reached a constant velocity.

4.4 Variation in Root Cutout

For the baseline case of a wing accelerating over one chord length and rotating to a maximum of 540 deg, root cutouts ranging from $0.25c$ to $2.50c$ were examined. The axis-relative Reynlods number was held constant at 10,000 regardless of the root cutout, as illustrated by Figure 2.8(a), which shows the Reynolds number distribution along the wing span for each root cutout tested. Figure 4.4 shows the lift and drag coefficients for all cases in this parameter sweep, with the reference plane defined using the axis-relative method (three quarters of the distance from the axis of rotation to the wing tip). The leftmost vertical dotted line indicates where the wing reached a constant velocity for all cases, and the remainder of the vertical dotted black lines indicate the beginning of wing deceleration for each case. Because the location of the axis-relative reference plane varies among the cases, there is not a constant relationship between s/c and rotation angle. As the root

cutout is increased, the axis-relative reference plane remains at 75% of the distance from the axis of rotation to the wing tip. However, this means that the spanwise location of the axis-relative reference plane moves toward the wing root as the root cutout is increased. For this reason, only s/c is plotted on the x-axis.

As evident from Figure 4.4, the force coefficients vary widely among the cases. For both lift and drag coefficients, the magnitude of the inertial peak is larger for larger root cutouts, as is the magnitude of the second local maximum. This is due to the fact that the spanwise velocity gradient seen by a rotating wing results in larger average velocity along the wingspan for larger root cutouts, where the root velocity is significantly higher. This is illustrated by Figure 4.3, reproduced from Section 2.3.2, which compares the local velocity along the wingspan for the $0.50c$ and $2.50c$ root-cutout cases. The velocity at the axis-relative reference plane remains constant among all root-cutout cases, and because the reference plane velocity is always 75% of the tip velocity, the tip velocity remains constant as well. However, when the root cutout is larger, the local velocity at the wing root is also larger. When converting dimensional forces into non-dimensional lift and drag coefficients, the axis-relative method normalizes forces using the velocity at the axis-relative reference plane. Thus, because the $2.50c$ root-cutout case has the largest local velocity at the wing root, and hence, the largest average velocity along the wing span, even when forces are non-dimensionalized, lift and drag coefficients for that case are larger than cases with smaller root cutouts. Despite the initial variation in force coefficients among the cases, for root cutouts of $1.50c$, $2.00c$, and $2.50c$ after approximately 5 chord-lengths traveled, the lift and drag coefficients collapse, but the smaller root cutouts

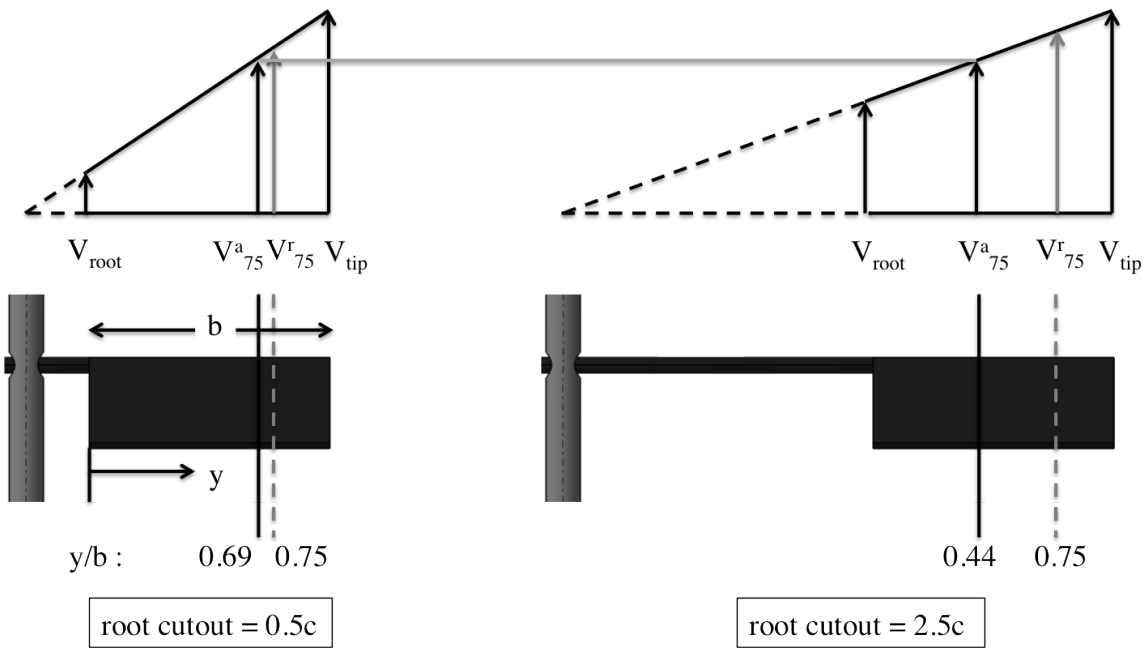

Figure 4.3: Comparison of spanwise local velocity for root cutouts of $0.50c$ and $2.50c$.

maintain smaller force coefficients throughout the 1.5 revolutions studied.

Because most insect wing stokes are limited to a maximum rotation angle of 180 deg, it is useful to examine more closely the lift and drag coefficients for $0° \leq \theta \leq 180°$ in more detail. Figure 4.5 shows the lift and drag coefficients from the start of wing rotation to a maximum stroke-to-chord ratio of 8.0, which corresponds to a rotation angle of 283 deg for a root cutout of $0.25c$, and 136 deg for a root cutout of $2.50c$. This figure more clearly shows that the local maximum that occurs at the end of wing acceleration, is larger for larger root cutouts. Figure 4.5 also shows that the difference in force coefficients among the cases grows smaller as s/c increases. By $s/c = 8.0$, the difference in the lift coefficient between $r_r = 0.25c$ and $r_r = 2.50c$ is 0.33, whereas the difference at $s/c = 1.0$ is 0.61.

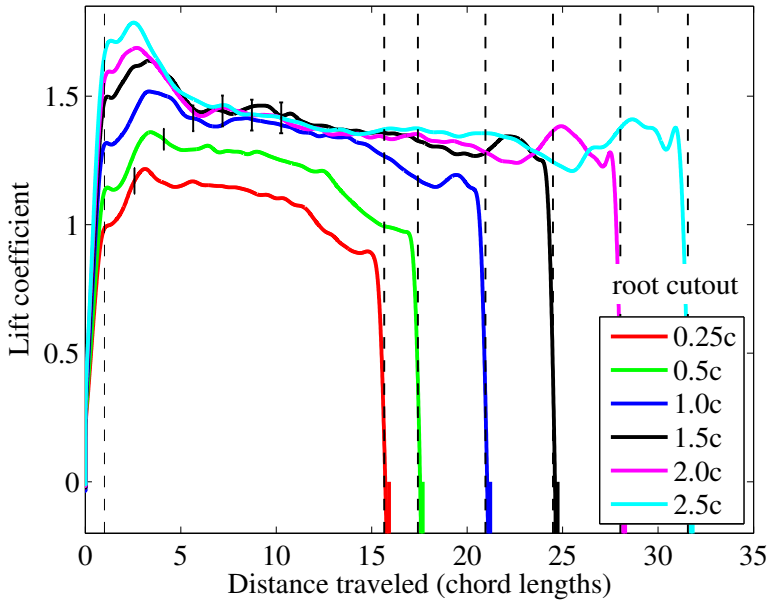

(a) Lift coefficient.

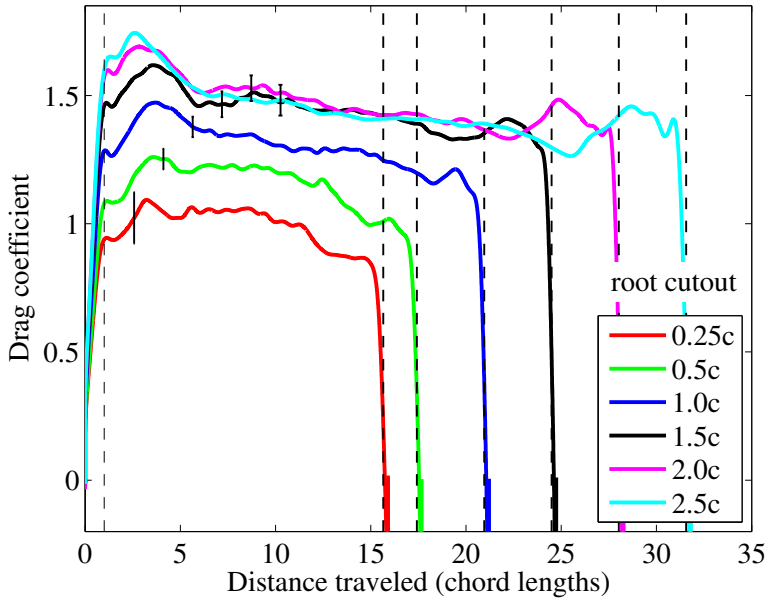

(b) Drag coefficient.

Figure 4.4: Axis-relative lift and drag coefficients for root cutouts of $0.25c$ (red), $0.50c$ (green), $1.00c$ (blue), $1.50c$ (black), $2.00c$ (magenta), and $2.50c$ (cyan).

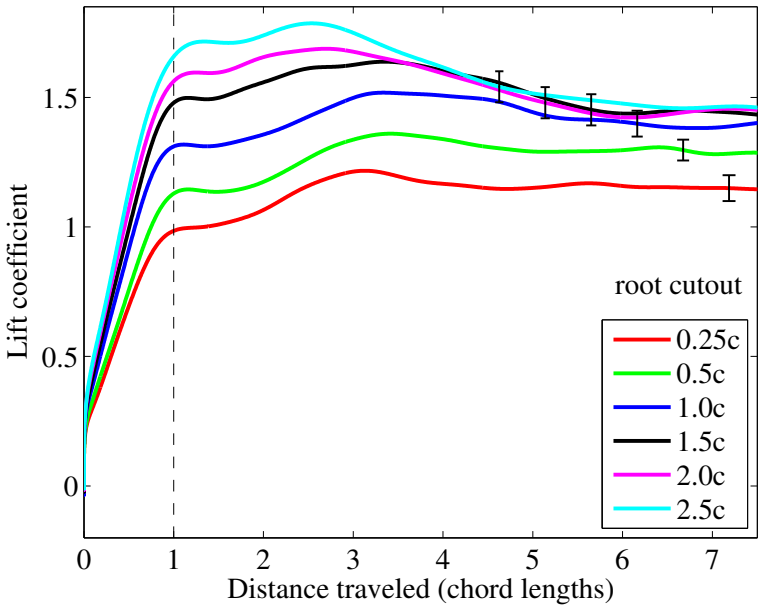

(a) Lift coefficient.

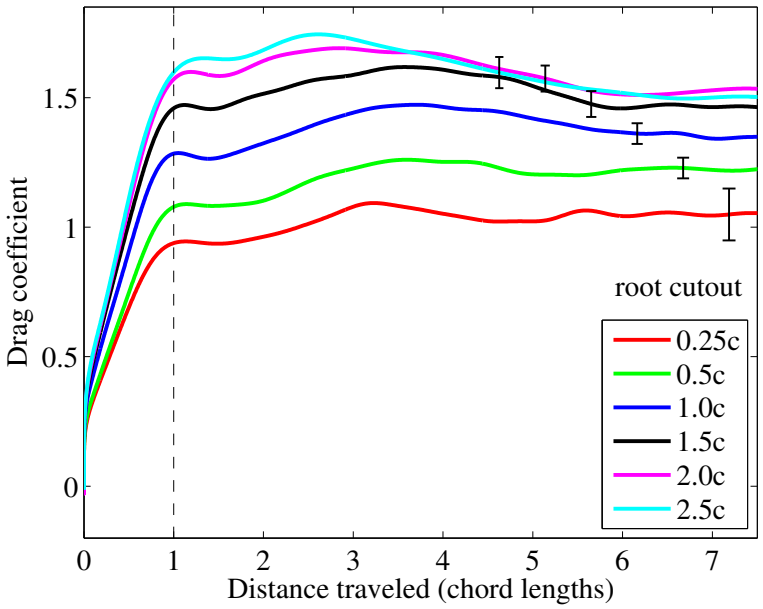

(b) Drag coefficient.

Figure 4.5: Axis-relative lift and drag coefficients for root cutouts of $0.25c$ (red), $0.50c$ (green), $1.00c$ (blue), $1.50c$ (black), $2.00c$ (magenta), and $2.50c$ (cyan).

Table 4.1: Root cutout vs. tip clearance.

Root Cutout	$0.25c$	$0.50c$	$1.00c$	$1.50c$	$2.00c$	$2.50c$
Tip Clearance	$3.0c$	$2.7c$	$2.2c$	$1.7c$	$1.2c$	$0.7c$

The acceleration and final rotation angle parameter sweeps resulted in a local maximum in force coefficients near $\theta = 90\,\text{deg}$ (see Figures 4.1 and 4.2), where the wingtip comes closest to the tank wall. Because the computational analysis showed that proximity to tank walls can artificially elevate lift and drag coefficients, one might suspect that the second local maximum was a result of wall effects, and not an inherent quality of the force coefficient histories. The root cutout parameter sweep provides a convenient way to determine if the second local maximum is in fact a result of wing proximity to the wall. From Figure 4.6, which plots the lift and drag coefficients vs. rotation angle, instead of s/c, it is evident that for smaller root cutouts, where the tip clearance is large, the second local maximum occurs at approximately 100 deg. However, for large root cutouts, the second local maximum occurs much earlier, around 50 deg. The exact values of root cutout and minimum tip clearance are given in Table 4.1. If wall effects were present, they would likely affect the forces around 90 deg or soon after, when the wing tip passes closest to a wall of the square tank. However, for a root cutout of $2.50c$, the second local maximum in the force coefficients occurs after just 50 deg, where the wing tip is furthest from a tank wall. This suggests that the second local maximum is not affected by the tank walls, and would occur even in an infinitely large tank.

The root-relative method of force normalization eliminates the effects of vari-

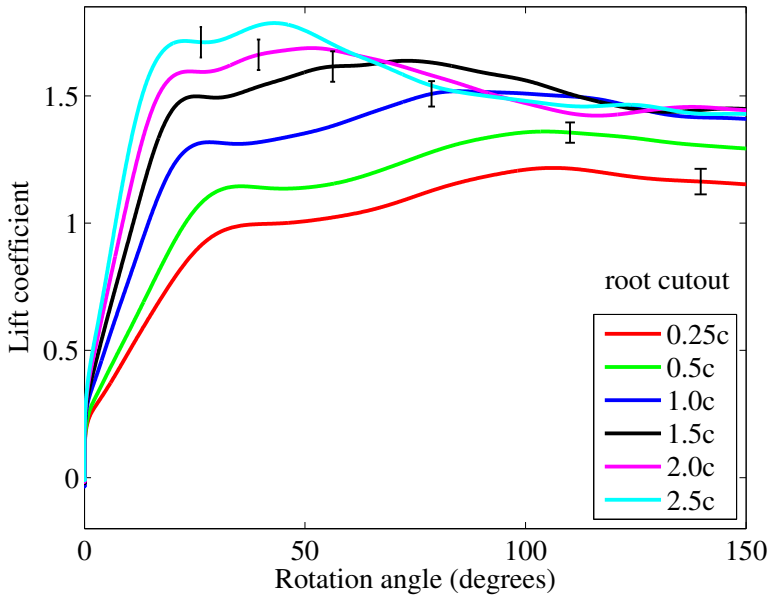

(a) Lift coefficient.

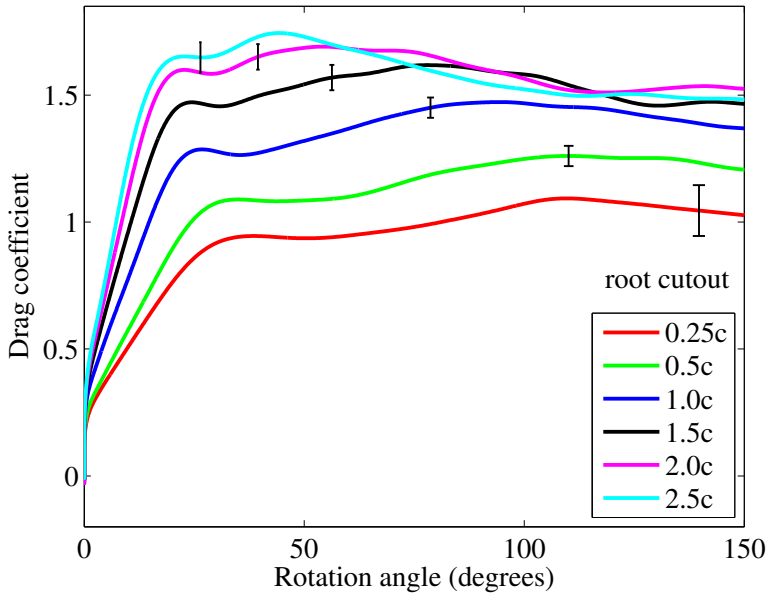

(b) Drag coefficient.

Figure 4.6: Axis-relative lift and drag coefficients for root cutouts of $0.25c$ (red), $0.50c$ (green), $1.00c$ (blue), $1.50c$ (black), $2.00c$ (magenta), and $2.50c$ (cyan) vs. rotation angle.

ations in average local velocity along the wing span by normalizing lift and drag by the integral of the local velocity, as described previously in Section 2.3.2. The lift and drag coefficients found by non-dimensionalizing in this manner are shown in Figure 4.7. In this figure, the non-circulatory peaks no longer align with $s/c = 1$, as they did when normalizing using the axis-relative method. This is because the velocity profiles were created such that the wing would accelerate over $1.00c$ measured at the reference plane defined according to the axis-relative method. Since the reference plane is at a different spanwise location for the root-relative method, the end of acceleration occurs at $1.02c$ for a root cutout of $0.25c$, and at $1.19c$ for a root cutout of $2.5c$.

Up to about $2.5c$ traveled, non-dimensionalizing lift and drag by this method collapses the lift and drag coefficient curves, eliminating the effects of variation in average local velocity along the wing span. However, for $s/c \geq 2.5c$, the force coefficient curves begin to diverge. Normalizing forces based on the integral of the velocity along the wingspan assumes a quasi-two dimensional flow, in which the lift produced by a given spanwise slice depends only on the the local flow velocity seen by that slice. This quasi-two-dimensional flow is a good approximation of the flow field early in the wing stroke, before the root and tip vortices develop. However, once these vortices develop, they will influence the lift produced by the wing, and the flow becomes highly three-dimensional. The divergence of the lift and drag coefficient curves around $2.5c$, as seen in Figure 4.7, suggests that this is point where the root and tip vortices have developed enough to affect the force coefficients. Additionally, the fact that the second local maximum (near $s/c = 3.3$ for a root cutout of $0.25c$)

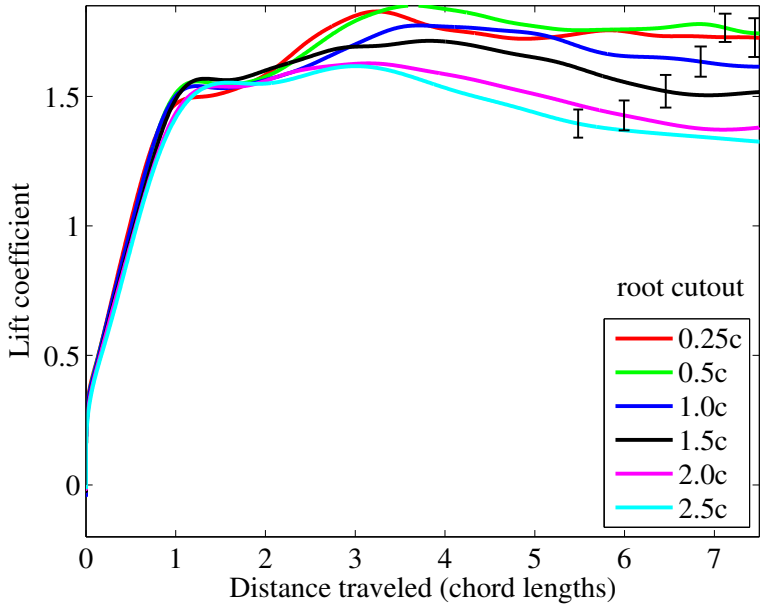

(a) Lift coefficient.

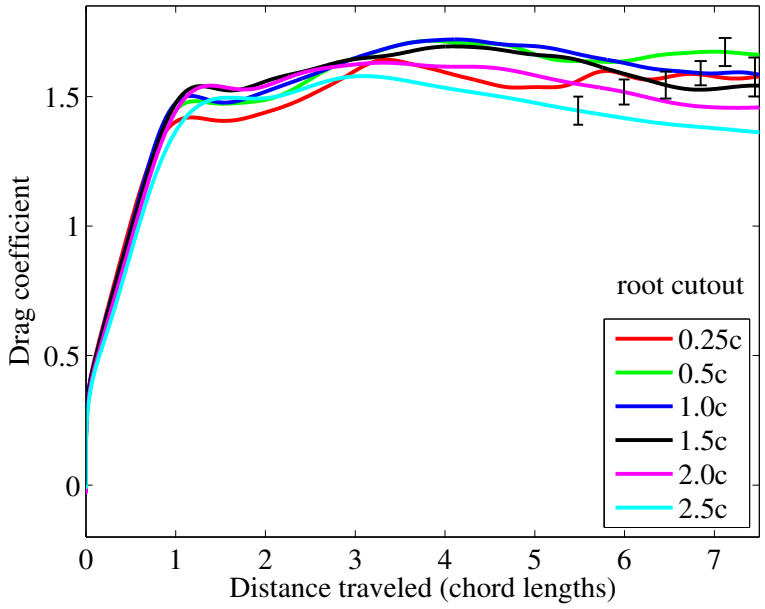

(b) Drag coefficient.

Figure 4.7: Root-relative lift and drag coefficients for root cutouts of $0.25c$ (red), $0.50c$ (green), $1.00c$ (blue), $1.50c$ (black), $2.00c$ (magenta), and $2.50c$ (cyan).

occurs after the force coefficient curves begin to diverge suggests that the root and tip vortices are responsible for the local increase in forces. Because the tip velocity is maintained at a constant value regardless of root cutout, it is reasonable to assume that the size and strength of the tip vortex is also similar despite variations in root cutout. Thus, the main difference in the three dimensionality of the flow arises from the strength of the root vortex. In cases where the root cutout, and as a result, the local velocity seen at the wing root, are large, the lift and drag coefficients are smaller between stroke-to-chord ratios of 2.5 and 8. This suggests that a stronger root vortex results in lower force coefficients.

4.5 Comparison with AFRL Data

In order to gain a better understanding of how to compare translating and rotating models of flapping flight, and to provide validation for the force data collected, correlated experiments were preformed in the Horizontal Free-Surface Water Tunnel at the Air Force Research Laboratory (AFRL), Wright-Patterson Air Force Base. The AFRL facility consists of a water tunnel with a test section that is 18 in wide and 24 in tall. No freestream was used for these experiments, so the water tunnel acted as a towing tank filled with quiescent water. The wing motion was controlled by three linear motors and a Galil DMC4040 4-channel card with variable proportional-integral-derivative (PID) constants for each channel. Two of the motors are mounted vertically. Their combined motion is capable of producing independent pitching and plunging motions for translating wing setups, and rota-

tion about any desired pivot point for the rotating wing setup. The third motor is mounted horizontally to produce a translational forward and backward motion. A more detailed description of the water tunnel facility can be found in Ref. [16].

4.5.1 Translating Wing Data

Because the insect wing stroke has been modeled by both rotating and translating wing experiments, it is essential to develop a basis on which to compare the results of such experiments. For this reason, rotating wing lift and drag coefficient histories for root cutouts ranging from $0.25c$ to $2.50c$, collected at UMD and analyzed using the root-relative method were compared to translating wing data acquired at AFRL.

The translating wing AFRL setup consists of an aspect ratio 2 flat plate wing at a fixed $\alpha = 45^{\circ}$ mounted on the plunge rods at mid-span of the pressure side of the plate. The Reynolds number for this experiment was 10,000 so as to match the rotating wing cases. Force measurements were taken using an ATI Nano17 IP-68 six degree-of-freedom load cell with the cylindrical axis of the load cell aligned with the spanwise direction of the wing.

Figure 4.8 shows a comparison of the lift and drag coefficients for the UMD root cutout parameter sweep and for the AFRL translating wing [43]. The rotating wing data was non-dimensionalized using the root-relative method. As the root cutout of a rotating wing becomes large, the velocity at the wing root increases. In the theoretical case of an infinitely large root cutout, the local velocity at the wing

root would equal that at the wing tip. This is identical to the case of a translating wing. Therefore, the force coefficients of the translating wing should most closely follow the case with the largest root cutout, especially once the three-dimensional effects introduced by the root and tip vortices become significant. The data shown in Figure 4.8 supports this hypothesis. From the beginning of wing motion until $2.5c$ traveled, the translating wing data is close to all of the rotating wing cases. After that point, the translating wing lift and drag coefficients are lower than those for all rotating wing cases, but are closest to the $2.5c$ root cutout case. Larger root cutouts would need to be examined to determine wether the observed trend of larger root cutouts yielding force coefficient curves that approach those of the translating wing.

4.5.2 Rotating Wing Data

In order to ensure that the data collected for this study is reliable, it is useful to compare results with those acquired in another facility. Rotating wing experiments were performed at AFRL that mimic the kinematics, aspect ratio, root cutout, Reynolds number, and other experimental parameters of the UMD $0.50c$ root cutout case. The AFRL rig was limited to a maximum of 90 deg of rotation due to mechanical constraints.

Figure 4.9 compares lift and drag coefficients for the UMD root cutout parameter sweep to lift and drag coefficients of the AFRL $0.5c$ root cutout rotating wing [44]. Aerodynamic forces from both datasets were non-dimensionalized using

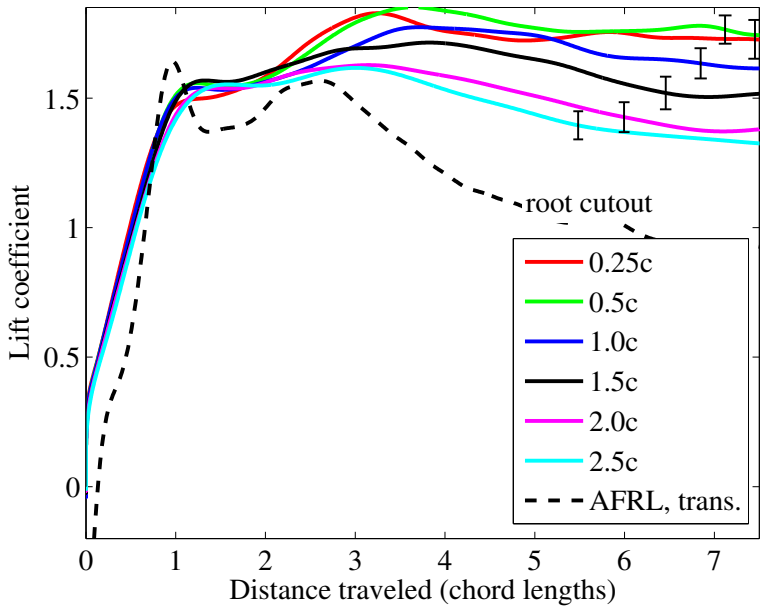

(a) Lift coefficient.

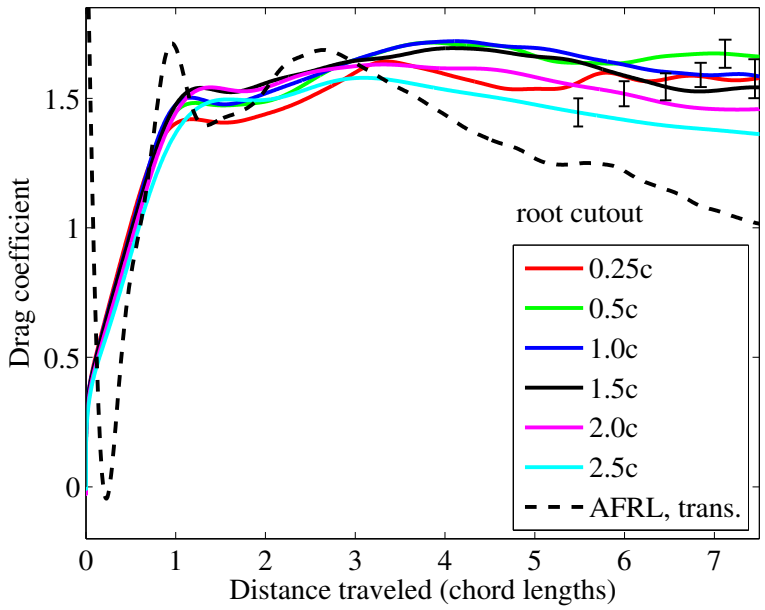

(b) Drag coefficient.

Figure 4.8: Root-relative lift and drag coefficients for root cutouts of $0.25c$ (red), $0.50c$ (green), $1.00c$ (blue), $1.50c$ (black), $2.00c$ (magenta), and $2.50c$ (cyan) with comparison to AFRL translating wing data (black, dotted line).

the axis-relative method. For the lift coefficient, the $0.50c$ root cutout case studied at UMD is very close to the rotating wing data collected at AFRL, which also has a root cutout of $0.5c$. However, the drag coefficient for the AFRL rotating wing is about 0.22 higher than the drag coefficient for the UMD $0.50c$ root cutout case. This could be due to a lack of taring out the inertial forces for the AFRL data.

4.6 Summary

Force data was acquired for rotating, fixed pitch wings in order to determine the effects of maximum rotation angle, acceleration profile, and root cutout on the lift and drag coefficient profiles. All force coefficient histories contained two local maxima in both lift and drag. The first, occurring at the end of wing acceleration, was a result of non-circulatory, or added mass, effects. The second local maximum, occurring at $s/c = 3.5$ ($\theta = 107°$) for a root cutout of $0.50c$, is thought to be associated with the development of the root and tip vortices.

Maximum rotation angle was found to have no effect on the force coefficient histories prior to the start of wing deceleration. Varying the distance over which a wing accelerated had resulted in larger non-circulatory peaks for shorter acceleration distances, which correspond to higher accelerations. However, after the wing reached a constant velocity, acceleration profile had no effect on the lift and drag coefficients.

Varying the root cutout affected both the magnitude and location of the second local maximum. Non-dimensionalizing forces by the root-relative method, as opposed to the axis-relative method, resulted in lift and drag coefficient histories

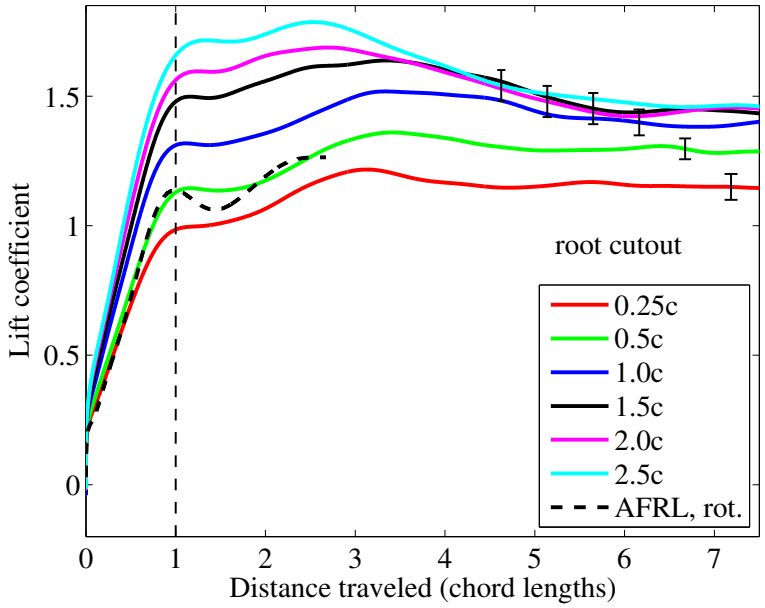

(a) Lift coefficient.

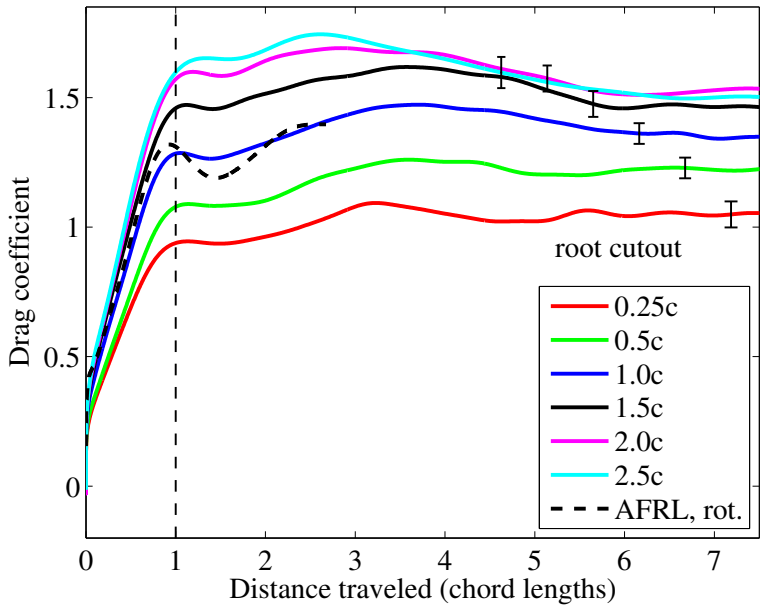

(b) Drag coefficient.

Figure 4.9: Axis-relative lift and drag coefficients for root cutouts of $0.25c$ (red), $0.50c$ (green), $1.00c$ (blue), $1.50c$ (black), $2.00c$ (magenta), and $2.50c$ (cyan) with comparison to AFRL $0.5c$ root cutout rotating wing data (black, dotted line).

that were independent of root cutout up to approximately $s/c = 2.5$. For $s/c > 2.5$, the force coefficient histories diverged. Comparing rotating wing lift and drag coefficients to data collected for a translating wing at AFRL showed that the translating wing force coefficients most closely aligned with force coefficients for the case with the largest root cutout. For more analysis of the effect of root cutout on the force coefficients of rotating wings see Ref. [45].

Chapter 5

Concluding Remarks

5.1 Overview

The focus of this study was to examine a variety of parameters affecting the flowfield and aerodynamic forces of wings rotating at low Reynolds numbers, including the effects of solid wall boundaries. This was approached computationally, so that the case where no wall boundaries are present could be simulated in addition to several discrete values of tip clearance. Particle/laser flow visualization was also performed to study the development of the large scale structures produced in an enclosed tank by a rotating wing. The flow visualization also aided in assessing the influence of the top and bottom walls of a tank on the flowfield of the rotating wing. The effects of maximum rotation angle, acceleration distance, and root cutout on the aerodynamic forces of a rotating wing were studied experimentally. Two different methods for determining Reynolds number and non-dimensionalizing lift and drag were compared, the root-relative method and the axis-relative method. Data collected at UMD was compared to rotating and translating wing data collected at AFRL.

5.2 Conclusions of the Study

5.2.1 Boundary Study Ananlysis

1. Several major flow features associated with a rotating wing were evident from chordwise and spanwise slices of Q-criterion taken at a variety of rotation angles. These include a large leading edge vortex, extending along the whole span of the wing. Also present were tip and root vortices, and a starting vortex shed from the trailing edge soon after the start of rotation. For all boundary cases, the size of the leading edge vortex decreased between the first and the second revolution. When comparing images of Q-criterion contours at a given rotation angle, it was difficult to discern any significant differences between the flowfields produced under various boundary conditions.

2. There were notable differences among the various boundary condition cases in the lift and drag coefficient histories. Both lift and drag coefficients for the $5.0c$ boundary case were approximately 7% higher than in the infinite case. In the first revolution, the $3.0c$ and $0.5c$ cases also had lift and drag coefficients that were 7% higher than for the infinite case, although the difference increased in the second revolution. When the wing entered the second revolution, all lift and drag coefficients dropped due to the wing encountering the wake produced in the first revolution. However, the force coefficients for the $0.5c$ case dropped significantly less than for the other three cases, resulting in an artificially elevated lift and drag coefficients throughout the second revolution.

3. The magnitude of the circulation contained in the LEV through a slice at half span was plotted as a function of rotation angle for all cases. In general, the trends observed in the LEV growth history were the same as those for the lift coefficient history. In the first revolution, the LEV circulation for the infinite case was slightly less than for the other three cases, which were all very similar. In the beginning of the second revolution the LEV circulation dropped for all cases, but dropped significantly less for the $0.5c$ case than for the other three cases.

4. The downwash created by the wake of the wing was quantified by plotting the vertical velocity one chord-length in front of the wing midspan. After 94 deg, the $0.5c$ boundary case had a higher downwash (4.6% of the tip velocity) than the other three cases (3.1% of the tip velocity). After 634 degrees, the maximum downwash for the $0.5c$ case was less than that of the other cases (9% of the tip velocity for $0.5c$ case, 25% for $5.0c$ and infinite cases). This suggests that downwash created by the wake lowers the effective angle of attack of the wing and decreases lift, and that this effect is suppressed by walls close to the wing tip.

5. Flow visualization of the tank cross-section showed that a rotating wing produces a ring-like vortex that coincides with the path swept out by the wing tip. This vortex grows larger as the wing travels for greater numbers of revolutions, until it impinges on the tank walls. Subsequently, a second, counter-rotating ring vortex is formed under the first, which eventually grows to occupy the

space between the primary ring vortex and the bottom of the tank. After two revolutions, none of the major flow structures for any of the three tip clearances studied (d_b =0.5c, 3.0c, and 5.0c) had yet impinged on the bottom of the tank.

6. For maximum rotation angles of less than one revolution, even a very small tip clearance of 0.5c is sufficient for preserving the trends in force histories and the flow features associated with a wing rotating in an infinitely large volume of fluid. However, for maximum rotation angle of two revolutions, a minimum tip clearance of 5.0c is necessary to preserve the characteristics of the infinite boundary condition case.

5.2.2 Force Measurement Analysis

1. Two local maxima were observed in the lift and drag coefficients for all cases. The first, occurring at the end of wing acceleration, is the result of non-circulatory, or added mass effects. The second local maximum occurs after 3.5c for a root cutout of 0.5c, and is likely due to the development of the root and tip vortices.

2. Varying the maximum rotation angle had no effect on the lift and drag coefficients of a rotating wing prior to wing deceleration. This is because the velocity profile for different maximum rotation angles is identical before the wing begins to decelerate.

3. Acceleration distance did not affect the force coefficients after the wing reached

a constant velocity. For the wing accelerating over $6.00c$, the second local maximum in forces was not observed. The wing was still accelerating when this peak would have otherwise occurred, which suggests that the flow features associated with the peak in lift are not present during wing acceleration, but only after the wing has reached a constant velocity.

4. Varying root cutout was found to have a significant effect on the location of the second local maximum in force coefficients. For a root cutout of $0.25c$, the peak was located at $s/c = 3.1$ ($\theta = 106°$), and for a root cutout of $2.5c$, the peak was located at $s/c = 2.5$ ($\theta = 43°$). The main difference between the flow over a wing with a small root cutout and a large root cutout for a given Reynolds number is the velocity at the wing root. Presumably, in cases where the root cutout is large, the root vortex develops sooner, and this is responsible for an earlier peak in forces.

5. When non-dimensionalizing aerodynamic forces using the axis-relative method, a variation in average velocity along the wing span among various cases resulted in significantly larger lift and drag coefficients for larger root cutouts. Non-dimensionalizing forces using the root-relative method took into account this variation and collapsed both lift and drag coefficients for $s/c \leq 2.0$. Therefore, the root-relative method of force normalization is better for comparing cases with varying root cutouts. At larger values of s/c, increased three dimensional effects resulted in a divergence of the root-relative lift and drag coefficients from each other.

6. Lift and drag coefficients normalized using the root-relative method for root cutouts ranging from $0.25c$ to $2.50c$ were plotted with force coefficients of a translating wing. The translating wing data most closely aligned with the $2.50c$ case. As the root cutout became large, the difference between the tip velocity and the root velocity got smaller, making the spanwise velocity distribution of the rotating wing more similar to a translating wing.

5.3 Remarks for Future Work

There are several avenues for further study that would be interesting to pusue given the results of this investigation. One other boundary case should be modeled computationally, with a finite tip clearance greater than $5.0c$. Although the flow features for the $5.0c$ case and the infinite case are very similar for up to two revolutions, the lift and drag coefficients for these cases are not identical. The boundary study performed computationally should be repeated experimentally for tip clearances of $0.5c$, $3.0c$, and $5.0c$ in order to confirm the computational results. Additionally, because Reynolds numbers seen in insect flight range from 100 to tens-of-thousands, it would also be useful to perform a Reynolds number parameter sweep to determine the effects of Reynolds number on force coefficients and flowfields of rotating wings. This will also help to determine wether the boundary study performed at a Reynolds number of 120 is applicable to higher Reynolds number cases.

The root cutout parameter sweep performed in water should be repeated in a glycerin water mixture. The increased kinematic viscosity of the fluid will amplify

the aerodynamic forces and potentially increase the signal to noise ratio of the data. Although the signal to noise ratio in the data presented here yielded relatively small error ranges, it would be interesting to see if this could be improved. Also, running these experiments in a fluid with a different viscosity will aid in proving that as long as Reynolds number is maintained, the results of these experiments can be replicated through proper scaling of wing size and rotational velocity.

Although hypothesized that the development of the root and tip vortices is responsible for the second local maximum in the force coefficients, this claim has yet to be validated. Particle image velocimetry and flow visualization would aid in determining the flow features associated with this peak.

Bibliography

[1] Aerovironment. UAS advanced development: Black widow. `http://www.avinc.com/uas/adc/black_widow/`, 2013. [Online; accessed 30 May-2013].

[2] Hrishikeshavan, V., Sirohi, J., Tishchenko, M., and Chopra, I. Design, development, and testing of a shrouded single-rotor micro air vehicle with antitorque vanes. *Journal of the American Helicopter Society*, 56(1):12008–1–12008–11(11), January 2011.

[3] S. A. Ansari, R. Żbikowski, and K. Knowles. Aerodynamic modelling of insect-like flapping flight for micro air vehicles. *Progress in Aerospace Sciences*, 42(2):129–172, February 2006.

[4] Ellington, C. P. The aerodynamics of hovering insect flight, I. The quasi-steady analysis. *Philosophical Transactions of the Royal Society of London, Series B, Biological Sciences*, 305(1122):41–78, February 1984.

[5] Sane, S. P. and Dickinson, M. H. The control of flight force by a flapping wing: Lift and drag production. *Journal of Experimental Biology*, 204:2607–2626, 2001.

[6] Lehmann, F. O. and Pick, S. The aerodynamic benefit of wing-wing interaction depends on stroke trajectory in flapping insect wings. *Journal of Experimental Biology*, 210:1362–1377, 2007.

[7] Hendrick, T. A hawk moth (manduca sexta) hovering in front of and preparing to feed from an artificial flower. `http://www.unc.edu/~thedrick/movies.html`, 2010. [Online; accessed 23 May-2013].

[8] Eldredge, J. D., Wang, C., and Ol, M. V. A computational study of a canonical pitch-up, pitch-down wing maneuver. In *39th AIAA Fluid Dynamics Conference*, AIAA 2009-3687, San Antonio, TX, 22-25 June 2009.

[9] Jones, A. R. and Babinsky, H. Unsteady lift generation on rotating wings at low Reynolds numbers. *Journal of Aircraft*, 47(3):1013–1021, 2010.

[10] DeVoria, A., Mahajan, P., and Ringuette, M. Vortex formation and saturation for low-aspect-ratio rotating flat plates at low reynolds number. In *49th AIAA Aerospace Sciences Meeting and Exhibit*, AIAA 2011-396, Orlando, FL, 4-7 January 2011.

[11] Lentink, D. and Dickinson, M. H. Rotational accelerations stabilize leading edge vortices on revolving fly wings. *Journal of Experimental Biology*, 212:2705–2719, April 2009.

[12] Ringuette, M., Milano, M., and Gharib, M. Role of the tip vortex in the force generation of low-aspect-ratio normal flat plates. *Journal of Fluid Mechanics*, 581:453–468, 2007.

[13] Jones, A. R., Pitt Ford, C., and Babinsky, H. Three-dimensional effects on sliding and waving wings. *Journal of Aircraft*, 48(2):633–644, 2011.

[14] Pitt Ford, C. and Babinsky, H. Low Reynolds number experiments on an impulsively started flat plate at high incidence. In *49th AIAA Aerospace Sciences Meeting and Exhibit*, AIAA 2011-475, Orlando, FL, 4-7 January 2011.

[15] Ol, M. V., Bernal, L., Kang, C. K., and Shyy, W. Shallow and deep dynamic stall for flapping low Reynolds number airfoils. *Experiments in Fluids*, 46:883–901, April 2009.

[16] Granlund, K., Ol, M. V., Bernal, L., and Kast, S. Experiments on free-to-pivot hover motions of flat plates. In *40th AIAA Fluid Dynamics Conference and Exhibit*, AIAA 2011-4456, Chicago, Il, 28 June - 1 July 2010.

[17] Kolluru Venkata, S. and Jones, A. R. Effects of acceleration and pitch variations on a rotating wing. In *50th AIAA Aerospace Sciences Meeting and Exhibit*, AIAA 2012-0050, Nashville, TN, 9-12 January 2012.

[18] Ellington, C. P. The aerodynamics of hovering insect flight, IV. Aerodynamic mechanisms. *Philosophical Transactions of the Royal Society of London, Series B, Biological Sciences*, 305(1122):79–113, February 1984.

[19] Weis-Fogh, T. Energetics of hovering flight in hummingbirds and drosophila. *Journal of Experimental Biology*, 56:79–104, 1972.

[20] Dickinson, M. H. and Götz, K. G. Unsteady aerodynamic performance of model wings at low Reynolds numbers. *Journal of Experimental Biology*, 174(1):45–64, January 1993.

[21] Dudley, R. and Ellington, C.P. Mechanics of forward flight in bumblebees ii. quasi-steady lift and power requirements. *Journal of Experimental Biology*, 148:53–88, 1990.

[22] Maxworthy, T. Experiments on the Weis-Fogh mechanism of lift generation by insects in hovering flight, I. Dynamics of the 'fling'. *Journal of Fluid Mechanics*, 93(1):47–63, July 1979.

[23] Wagner, H. Über die Entstehung des dynamischen Äuftriebes von Tragflügeln. *Zeitschrift für Angewandie Mathematik und Mechanik*, 5(1):17–35, 1925.

[24] Jones, R. T. Operational treatment of the non-uniform lift theory in airplane dynamics. Technical Note 667, NASA, 1938.

[25] Garrick, I.E. On some reciprocal relations in the theory of nonstationary flows. Technical Note 629, NACA, 1938.

[26] Leishman, J. G. *Principles of Helicopter Aerodynamics*. Cambridge University Press, Cambridge, United Kingdom, 2nd edition, 2006.

[27] Francis, R. H. and Cohen, J. The flow near a wing which starts suddenly from rest and then stalls. *Rep. Memo. Aeronaut. Res. Comm.*, no. 1561, 1933.

[28] McCroskey, W. J. Unsteady airfoils. *Annual Review of Fluid Mechanics*, 14:285–311, 1982.

[29] Van Dyke, M. *An Album of Fluid Motion*. The Parabolic Press, Stanford, CA, 1982.

[30] Dickinson, M. H., Lehmann, F. O., and Sane, S. P. Wing rotation and the aerodynamic basis of insect flight. *Science*, 284(5422):1954–1960, 18 June 1999.

[31] Pitt Ford, C. and Babinsky, H. Lift and the leading edge vortex. In *50th AIAA Aerospace Sciences Meeting and Exhibit*, AIAA 2012-0991, Nashville, TN, 9-12 January 2012.

[32] Jones, A. R. and Babinsky, H. Reynolds number effects on leading edge vortex development on a waving wing. *Experiments in Fluids*, 51(1):197–210, 2011.

[33] Kolluru Venkata, S. and Jones, A. R. Leading edge vortex structure over multiple revolutions of a rotating wing. *to appear in Journal of Aircraft*, 2013.

[34] Ozen, C.A. and Rockwell, D. Flow structure on a rotating plate. *Experiments in Fluids*, 52(1):207–223, 2011.

[35] Kim, D. and Gharib, M. Experimental study of three-dimensional vortex structures in translating and rotating plates. *Experiments in Fluids*, 49:329–339, April 2010.

[36] Wojcik, C. and Buchholtz, J. The dynamics of spanwise vorticity on a rotating flat plate. In *50th AIAA Aerospace Sciences Meeting and Exhibit*, AIAA 2012-0050, Nashville, TN, 9-12 January 2012.

[37] Bush, B. L. and Baeder, J. Computational investigation of flapping-wing flight. In *37th AIAA Fluid Dynamics Conference and Exhibit*, Miami, FL, 25-28 June 2007.

[38] Bush, B. L., MacFarlane K., Baeder, J., and Humbert, J. S. Development of immersed boundary code with application to mav stability analysis. In *27th Army Sciences Conference*, Orlando, FL, 29 November - 2 December 2010.

[39] Ellington, C. P., van den Berg, C., Willmott, A. P., and Thomas, A. L. R. Leading-edge vortices in insect flight. *Nature*, 384(6610):626–630, December 1996.

[40] Birch, J. M., Dickinson, W. H., and Dickinson, M. H. Force production and flow structure of the leading edge vortex on flapping wings at high and low reynolds numbers. *Journal of Experimental Biology*, 207(7):1063–1072, March 2004.

[41] Haller, G. An objective definition of a vortex. *Journal of Fluid Mechanics*, 525(1):1–26, February 2005.

[42] Graftieaux, L., Michard, M., and Grosjean, N. Combining PIV, POD and vortex identification algorithms for the study of unsteady turbulent swirling flows. *Measurement Science and Technology*, 12(9):1422–1429, August 2001.

[43] Granlund, K. AFRL translating wing data. personal communication, 2012.

[44] Granlund, K. AFRL rotating wing data. personal communication, 2013.

[45] Schlueter, K., Jones, A. R., Granlund, K., and Ol, M.V. The effect of root cutout on the force coefficient of rotating wings. *submitted to AIAA Journal*, 2013.